行政院國家科學委員會專題研究計畫 成果報告

發展有限元素數值模型以研究新型光電結構(II)
研究成果報告(精簡版)

計 畫 類 別 ：個別型
計 畫 編 號 ：NSC 95-2221-E-002-328-
執 行 期 間 ：95 年 08 月 01 日至 96 年 07 月 31 日
執 行 單 位 ：國立臺灣大學電信工程學研究所

計 畫 主 持 人：張宏鈞

計畫參與人員：博士班研究生-兼任助理：許森明、劉暄浩
碩士班研究生-兼任助理：葉涵之、鍾長均

處 理 方 式 ：本計畫可公開查詢

中 華 民 國 96 年 12 月 13 日

行政院國家科學委員會專題研究計畫成果報告

發展有限元素數值模型以研究新型光電結構(II)

Development of finite Element Numerical Models for Research on Novel Photonic Structures (II)

計畫編號：NSC 95-2221-E-002-328
執行期限：95 年 8 月 1 日至 96 年 7 月 31 日

主持人：張宏鈞　台灣大學電機系、光電所暨電信所教授
計畫參與人員：許森明(台大光電所)　劉暄浩(台大光電所)
葉涵之(台大電信所)　鍾長均(台大光電所)

一、中文摘要

本計畫已建立可分析具各向異性材質波導的全向量有限元素法模態解法，採用曲線性複合邊界結點三角形元素以及完全匹配層吸收邊界，包括三維的有限元素波束傳播法以及虛軸波束傳播法，並推展至材質具非線性特性的非線性波導之計算。本計畫並成功以有限元素法計算具非對角化各向異性材質的二維光子晶體能隙結構，並討論其完整的能隙結構分析。另外，也提出一項虛軸波束傳播法，結合有限元素法，可計算相關能帶問題。針對具有金屬材質之三角凸楔形結構的表面電漿子模態，本計畫亦已完成詳細的分析。

關鍵詞：光波導、各向異性波導、非線性光波導、光子晶體、有限元素法、波束傳播法、表面電漿子波導

Abstract

In this research we have developed full-vectorial finite element method (FEM) mode solvers for analyzing waveguides with arbitrary material anisotropy. The solves are based on curvilinear hybrid edge/nodal elements with triangular shape and are incorporated with perfectly matched layer (PML) absorbing boundaries. The solvers include the three-dimensional (3-D) beam propagation method (BPM) version and the imaginary-distance BPM version and have been generalized to the analysis of nonlinear optical waveguides involving nonlinear materials. We have also successfully used the FEM to compute band diagrams for 2-D photonic crystals having non-diagonal material anisotropy and discussed the complete analysis of such band diagrams. In addition, an imaginary-axis BPM combined with the FEM has been proposed, which is useful to band-diagram calculation. We have also completed detailed analysis of surface plasmon modes on triangular metal wedge structures.

Keywords: Optical waveguides, anisotropic waveguides, nonlinear optical waveguides, photonic crystals, finite element method, beam propagation method, surface plasmon waveguides

二、計畫緣由與目的

本計畫延續上年度工作，以有限元素法為基礎，發展高準度的波導模態分析數值模型，以輔助研發及設計各種特殊的光導波結構，並推展至材質具非線性特性的非線性波

導之計算。本計畫將原建立的採用曲線性複合邊界結點三角形元素的全向量有限元素法推展至任意各向異性波導材質的情況，維持完全匹配層吸收邊界，並建立了三維的有限元素波束傳播法以及虛軸波束傳播法，對於波導模態的分析可視不同的結構，選擇採用特徵值問題模態解法或虛距波束傳播法，此部分的詳細內容已於上年度報告中詳述。本年度應用之一例為詳細分析次波長尺度的光子線(photonic wire)波導在不同結構參數與波長下之向量模態與洩漏特性，並在國際研討會發表[1]。本計畫並成功以有限元素法計算具非對角化各向異性材質的二維光子晶體能隙結構，並討論其完整的能隙結構分析，補足前人討論的不完整[2], [3]。另外，也提出一項虛軸波束傳播法，結合有限元素法，可計算相關能帶問題[4]。針對具有金屬材質之三角凸楔形結構的表面電漿子模態，本計畫亦已完成詳細的分析[5]。本報告根據以有限元素法計算具非對角化各向異性材質的二維光子晶體能隙結構、虛軸有限元素波束傳播法的發展、具有金屬材質之三角凸楔形結構的表面電漿子模態之分析以及非線性光波導之研究等四部分分別說明研究成果。

三、結果與討論

1. 以有限元素法計算具非對角化各向異性材質的二維光子晶體能隙結構

計算光子晶體的能隙結構，目前最廣被採用的方法為平面波展開法，以有限元素法計算能隙結構的文章很少見，以類似有限元素光波模態解法，我們可推導出 E_z 與 H_z(垂直於二維光子晶體平面)的 Helmholtz 方程式，分屬橫向磁場波與橫向電場波，計算區域為單一晶包(unit cell)內，然後採用週期性邊界條件於同方向的邊界，得到所需的特徵值問題。建立有限元素解法的主要目的之一為，在已建立的可處理各向異性材質的有限元素法基礎之上，很容易可建立計算具各向異性材質光子晶體能隙結構的模型。本計畫已完成計算與研究 permittivity tensor 為平面非對角化之材質(如液晶的光軸落於二維光子晶體平面上)的能隙結構，討論重點為須仔細分析 first Brillouin zone 的每一 sub-zone 方能獲得完整能隙結構，這是他人論文未考慮完整的，請參 Appendix I (發表於 Optics Express 期刊的論文[2])。

2. 虛軸有限元素波束傳播法的發展

我們提出一項求解 Helmholtz 方程式的新穎的波束傳播法，將分析光子晶體能帶的 Helmholtz 方程式 $\frac{\partial^2\tilde{\Psi}}{\partial x^2}+\frac{\partial^2\tilde{\Psi}}{\partial z^2}+\omega^2\mu\varepsilon\tilde{\Psi}=0$ 寫成 $-\omega^2\tilde{\Psi}=\frac{1}{\mu\varepsilon}\left(\frac{\partial^2\tilde{\Psi}}{\partial x^2}+\frac{\partial^2\tilde{\Psi}}{\partial z^2}\right)$，再將 ω^2 以 ω' 取代，經由傅立葉轉換可形成一類似熱方程的形式，與前述波束傳播法的方程式相似，因此可藉由類似虛距波束傳播法求得 ω'，因而得到 Helmholtz 方程式中的特徵值 ω^2 以及其場型。以波束傳播法方式算光子晶體能帶，乃是創新方式，我們稱之為虛軸波束傳播法(imaginary-axis beam propagation method)，在 x-y 平面的求解方式係採用有限元素法，得以計算相關能帶問題，請參 Appendix II (發表於 WFOPC 2007 國際研討會的論文[4])。

3. 具有金屬材質之三角凸楔形結構的表面電漿子模態之分析

本計畫採用複合邊界結點三角形元素的全向量有限元素法程式分析具有金屬材質利用表面電漿子(surface plasmon)現象的光波導, 例如全金屬材質三角形凹槽尖角處可形成模場局限，構成極細的光波導，且特性與凹槽夾角大小有關，有製作高密度光線路的潛力，而三角凸楔形結構頂端尖角處也可形成模場局限。文獻中有採用有限差分時域法法分析相關結構者，精準度有限，本研究以有限元素法精確計算三角凸楔形結構頂端尖角處表面電漿子模態之模場與損耗特性，詳細探討頂端尖角角度對模場特性的影響，於日本的研討會發表一篇邀請論文，請參 Appendix III (發表於 2007 Japan-Indo Workshop on Microwaves, Photonics, and Communication Systems 的論文[5])。

4. 非線性光波導之研究

當光波導的材質具非線性特性，其折射率會隨光強度而變化，即形成非線性波導，是非線性光學中一個基本的課題。以光纖為例，其色散特性會因而隨光強度而改變。本計畫將有限元素波束傳播法模型推展至非線性波導結構的分析，以下為非線性光耦合器之一例。如圖一(a)所示，耦合器結構之參數為 $a = b = 2$ μm，$W_x = 12$ mm，$W_y = 4$ mm，$n_1 = 1.6$，$n_2 = 1.51$，導波區非線性係數為 $n' = 4.56 \times 10^{-11}$ m^2/W，導波區折射率與光強的關係為 $n = n_1 (1 + (n'/Z_0) |\boldsymbol{E}|^2)^{1/2}$，光波長為 1.523 μm，圖一(b)為有限元素分割圖。先以有限元素模態解法模型算出單一根波導的線性 quasi-TE 模場型，做為第一根波導的入射場型，再以有限元素波束傳播法模擬在不同功率下耦合器中的傳播現象，並計算第一根波導的輸出功率，在耦合器長度為 564 μm (等於線性耦合長度)時，正規化輸出功率隨輸入功率變化的情形示於圖二，與文獻結果[6]一致。

四、計畫成果自評

本計畫研究內容與原計畫相符，預期目標大致達成。本計畫將原建立的採用曲線性複合邊界結點三角形元素的全向量有限元素法推展至任意各向異性波導材質的情況，維持完全匹配層吸收邊界，並建立了三維的有限元素波束傳播法以及虛軸波束傳播法，得以研究許多種類的波導元件結構，包括次波長大小的光子線波導與金屬結構的表面電漿子模態，並推展至材質具非線性特性的非線性波導之計算。本計畫並成功以有限元素法計算具非對角化各向異性材質的二維光子晶體能隙結構，討論其完整的能隙結構分析。另外，也提出一項虛軸波束傳播法，結合有限元素法，可計算相關能帶問題。

五、參考文獻

[1] H. C. Chang, S. M. Hsu, and C. P. Yu, "Accurate Analysis of Modal and Leaky Characteristics of Silicon-on-Insulator Photonic Wires," presented at *Joint Session of the 13th European Conference on Integrated Optics (ECIO 2007) and XVI International Workshop on Optical Waveguide Theory and Numerical Modelling (OWTNM 2007)*, in *Proceedings of OWTNM 2007*, p. 59, Copenhagen, Denmark, April 25–28, 2007.

[2] S. M. Hsu, M. M. Chen, and H. C. Chang, "Investigation of Band Structures for 2D Non-diagonal Anisotropic Photonic Crystals Using a Finite Element Method Based Eigenvalue Algorithm," *(OSA) Optics Express*, Vol. 15, No. 9, pp. 5416–5430, 30 April 2007.

[3] S. M. Hsu, M. M. Chen, and H. C. Chang, "Band-Structure Analysis of 2D Non-Diagonal Anisotropic Photonic Crystals by the Finite Element Method," in *OSA 2006 Integrated Photonics and Nanophotonics Research and Applications (IPNRA '07) Technical Digest* (CD ROM), paper IMB2 (3 pages), Salt Lake City, Utah, July 8–11, 2007.

[4] S. M. Hsu, B. Y. Lin, and H. C. Chang, "A Finite-Element Imaginary-Time Beam Propagation Method for Two-Dimensional Photonic Crystal Analysis," *The 5th Workshop on Fibers and Optical Passive Components (WFOPC 2007)*, paper THP-20 (3 pages), Taipei, Taiwan, R.O.C., December 5–7, 2007.

[5] H. C. Yeh, C. H. Peng, B. Y. Lin, and H. C. Chang, "Modal Analysis of Plasmonic Waveguides," in *2007 Japan-Indo Workshop on Microwaves, Photonics, and Communication Systems Digest*, pp. 94–98, Kyushu University, Fukuoka, Japan, July 6, 2007. (**Invited paper**)

[6] T. Fujisawa and M. Koshiba, "Full-Vector Finite-Element Beam Propagation Method for Three-Dimensional Nonlinear Optical Waveguides," *J. Lightwave Technol.*, Vol. 20, pp. 1876–1884, 2002.

六、圖表

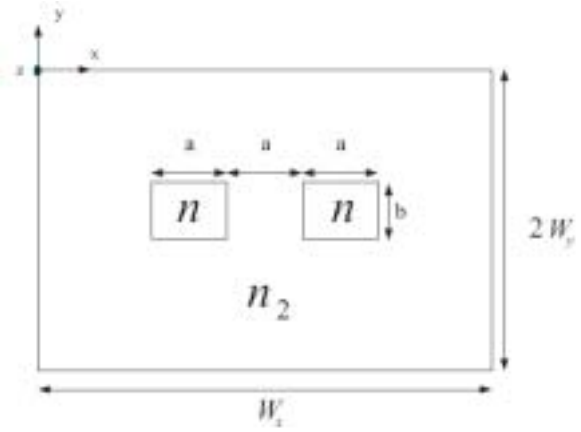

(a)

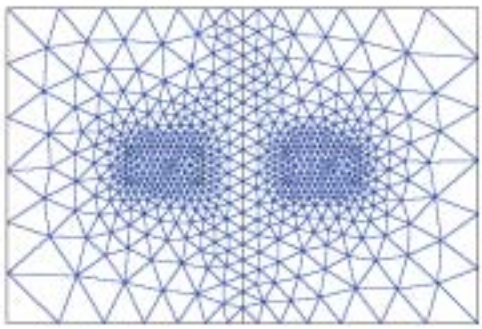

(b)

圖一 (a)非線性光耦合器的結構圖。(b)有限元素分割圖。

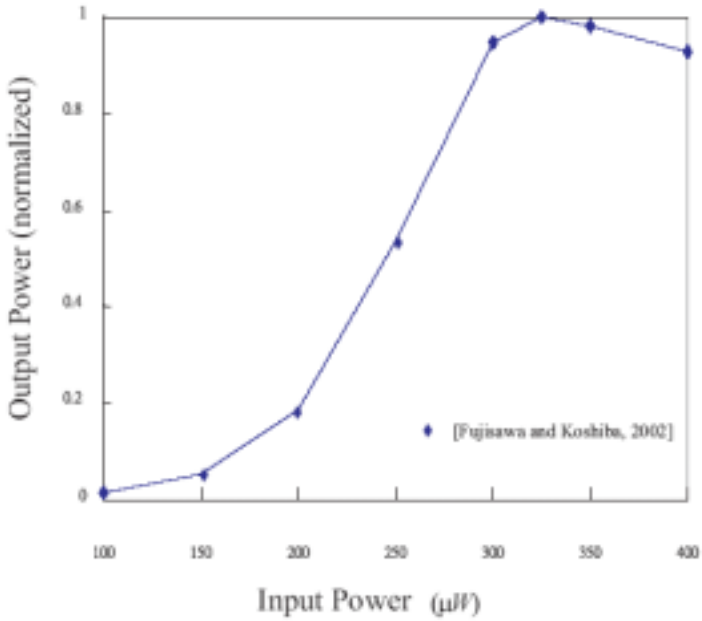

圖二 圖一之非線性光耦合器在左邊波導以 quasi-TE 模入射以及耦合器長度為 564 μm (等於線性耦合長度)時，左邊波導之正規化輸出功率隨輸入功率變化的情形。

Appendix I

Investigation of band structures for 2D non-diagonal anisotropic photonic crystals using a finite element method based eigenvalue algorithm

Sen-ming Hsu, Ming-mung Chen, and Hung-chun Chang[†]

Graduate Institute of Electro-Optical Engineering
National Taiwan University, Taipei, Taiwan 106-17, R.O.C.
[†]*also with the Department of Electrical Engineering and the Graduate Institute of Communication Engineering, National Taiwan University*

hcchang@cc.ee.ntu.edu.tw

Abstract: A finite element method based eigenvalue algorithm is developed for the analysis of band structures of two-dimensional non-diagonal anisotropic photonic crystals under the in-plane wave propagation. The characteristics of band structures for the square and triangular lattices consisting of anisotropic materials are examined in detail and the intrinsic effect of anisotropy on the construction of band structures is investigated. We discover some interesting relationships of band structures for certain directions of the wave vector in the first Brillouin zone and present a theoretical explanation for this phenomenon. The complete band structures can be conveniently constructed by means of this concept.

OCIS codes: (230.3990) Microstructure devices; (160.3710) Liquid crystals; (260.2110) Electromagnetic theory; (999.9999) Photonic crystals.

References and links

1. E. Yablonovitch, "Inhibited spontaneous emission in solid-state physics and electronics," Phys. Rev. Lett. **58**, 2059–2062 (1987).
2. S. John, "Strong localization of photons in certain disordered dielectric superlattices," Phys. Rev. Lett. **58**, 2486–2489 (1987).
3. J. D. Joannopoulos, R. D. Meade, and J. N. Winn, *Photonic Crystals: Molding the Flow of Light* (Princeton University Press, Princeton, NJ, 1995).
4. J. C. Knight, T. A. Birks, P. St. J. Russell, and D. M. Atkin, "All-silica single-mode optical fiber with photonic crystal cladding," Opt. Lett. **21**, 1547–1549 (1996).
5. S. G. Johnson, S. Fan, P. R. Villeneuve, J. D. Joannopoulos, and L. A. Kolodziejski, "Guided modes in photonic crystal slabs," Phys. Rev. B **60**, 5751–5758 (1999).
6. P. R. Villeneuve, S. Fan, and J. D. Joannopoulos, "Microcavities in photonic crystals: Mode symmetry, tunability, and coupling efficiency," Phys. Rev. B **54**, 7837–7842 (1996).
7. H. A. Haus, *Waves and Fields in Optoelectronics* (Prentice-Hall, Inc., Englewood Cliffs, NJ, 1984).
8. I. H. H. Zabel and D. Stroud, "Photonic band structures of optically anisotropic periodic arrays," Phys. Rev. B **48**, 5004–5012 (1993).
9. Z. Y. Li, B. Y. Gu, and G. Z. Yang, "Large absolute band gap in 2D anisotropic photonic crystals," Phys. Rev. Lett. **81**, 2574–2577 (1998).
10. C. Y. Liu and L. W. Chen, "Tunable band gap in a photonic crystal modulated by a nematic liquid crystal," Phys. Rev. B **72**, 045133 (2005).
11. M. Qiu and S. He, "A nonorthogonal finite-difference time-domain method for computing the band structure of a two-dimensional photonic crystal with dielectric and metallic inclusions," J. Appl. Phys. **87**, 8268–8275 (2000).

#79272 - $15.00 USD Received 22 Jan 2007; revised 14 Apr 2007; accepted 17 Apr 2007; published 19 Apr 2007

12. L. Zhang, N. G. Alexopoulos, D. Sievenpiper, and E. Yablonovitch, "An efficient finite-element method for the analysis of photonic band-gap materials," in 1999 IEEE MTT-S Dig. **4**, 1703–1706 (1999).
13. C. P. Yu and H. C. Chang, "Compact finite-difference frequency-domain method for the analysis of two-dimensional photonic crystals," Opt. Express **12**, 1397–1408 (2004).
14. P. J. Chiang, C. P. Yu, and H. C. Chang, "Analysis of two-dimensional photonic crystals using a multidomain pseudospectral method," Phys. Rev. E **75**, 026703 (2007).
15. G. Alagappan, X. W. Sun, P. Shum, M. B. Yu, and D. den Engelsen, "Symmetry properties of two-dimensional anisotropic photonic crystals," J. Opt. Soc. Am. A **23**, 2002–2013 (2006).
16. J. Jin, *The Finite Element Method in Electromagnetics* (John Wiley and Sons, Inc., New York, 2002).
17. M. Koshiba and Y. Tsuji, "Curvilinear hybrid edge/nodal elements with triangular shape for guided-wave problems," J. Lightwave Technol. **18**, 737–743 (2000).
18. P. Yeh and C. Gu, *Optics of Liquid Crystal Displays* (John Wiley and Sons, Inc., New York, 1999).

1. Introduction

Photonic crystals (PCs) are structures in which the materials are periodically organized to affect the propagation of electromagnetic (EM) waves. With the photonic band gaps (PBGs), the frequency ranges in which the EM waves are forbidden to propagate, resulting from the structure periodicity, PCs have inspired much interest and a lot of efforts have been devoted to their possible applications [1,2]. Among varieties of PCs, two-dimensional (2D) PCs, characterized by easy fabrication, have attracted special attention and have been widely employed in various applications such as PC fibers, waveguides, and photonic cavities [3–6]. Most of these applications make great use of the property of PBGs to achieve an extremely high degree of control over the propagation of EM waves. Consequently, accurate analyses of the band structures, and thus the PBGs, are quite significant for the design of these devices.

In addition to the spatial configuration of materials, material property itself plays a prominent role in the propagation of EM waves as well. The refractive index experienced by the EM wave propagating in isotropic materials is independent of the electric polarization, whereas that in anisotropic materials is strongly dependent on the electric polarization, which is further related to the wave propagation direction [7]. Hence, by introducing anisotropic materials into PCs, the band structures change and some interesting phenomena have been observed and studied [8–10]. However, the intrinsic effect on the concept of constructing the band structures caused by the introduction of anisotropic materials has not been discussed in any systematic way and is our main concern in this paper.

There are various kinds of numerical methods employed to calculate the band structures of 2D PCs. The plane-wave expansion (PWE) method [3] and the finite-difference time-domain (FDTD) method [11] are two usual schemes. In addition, the finite element method (FEM) [12] was utilized for this analysis likewise. Recently, the finite-difference frequency-domain (FDFD) method [13] and the pseudospectral method (PSM) [14] have also been demonstrated to provide alternative good approaches to obtain the band structures accurately. Most of these researches have focused on the structures made of either isotropic materials or anisotropic materials with diagonal permittivity and permeability tensors. But for many realistic applications, the principal coordinate system of the anisotropic materials may not always perfectly coincide with the coordinate system of the PCs [15]. Consequently, the development of a more general numerical model which takes non-diagonal permittivity and permeability tensors into consideration becomes a highly valuable issue. Based on this kind of numerical model, it becomes possible to fully understand how the anisotropy influences the band structures and correctly take advantage of anisotropy on the utilization of PBGs.

In this paper, an FEM based eigenvalue algorithm for the analysis of band structures of 2D PCs formed by anisotropic materials is accomplished. The formulation is generalized to be able to deal with non-diagonal permittivity and permeability tensors in the cross-sectional plane of the PC for the in-plane wave propagation. For better accuracy and efficiency, the curved geom-

#79272 - $15.00 USD Received 22 Jan 2007; revised 14 Apr 2007; accepted 17 Apr 2007; published 19 Apr 2007

etry in the structures is modeled by the curvilinear elements. The thorough derivation of this FEM based eigenvalue algorithm, including the adopted elements and the periodic boundary conditions (PBCs), is described in Section 2 in detail. Then the 2D anisotropic PCs with square and triangular lattices, composed of parallel silicon rods surrounded by liquid crystals (LCs) [10], are analyzed in Section 3. From these numerical results, we examine the relationships of band structures obtained from all possible directions of wave vector in the first Brillouin zone (BZ) and identify a guide for constructing the complete band structures of 2D anisotropic PCs. From these analyses we learn that the construction of band structures for anisotropic PCs have great differences from that for isotropic cases due to the intrinsic anisotropy which break the structure symmetry condition. The conclusion is summarized in Section 4.

2. Formulation

Under the source-free condition and with a time (t) dependence of the form $\exp(j\omega t)$ being implied, Maxwell's curl equations can be expressed as

$$\nabla \times \mathbf{E} = -j\omega\mu_0[\mu_r]\mathbf{H} \tag{1}$$

$$\nabla \times \mathbf{H} = j\omega\varepsilon_0[\varepsilon_r]\mathbf{E} \tag{2}$$

where ω is the angular frequency, μ_0 and ε_0 are the permeability and permittivity of free space, and $[\mu_r]$ and $[\varepsilon_r]$ are, respectively, the relative permeability and permittivity tensors of the medium given by

$$[\mu_r] = \begin{bmatrix} \mu_{xx} & \mu_{xy} & \mu_{xz} \\ \mu_{yx} & \mu_{yy} & \mu_{yz} \\ \mu_{zx} & \mu_{zy} & \mu_{zz} \end{bmatrix} \tag{3}$$

$$[\varepsilon_r] = \begin{bmatrix} \varepsilon_{xx} & \varepsilon_{xy} & \varepsilon_{xz} \\ \varepsilon_{yx} & \varepsilon_{yy} & \varepsilon_{yz} \\ \varepsilon_{zx} & \varepsilon_{zy} & \varepsilon_{zz} \end{bmatrix}. \tag{4}$$

For a 2D PC which is uniform along the z direction and periodic in the x-y plane, the wave modes in the PC for the in-plane propagation can be decoupled into transverse-electric (TE) and transverse-magnetic (TM) to z modes if the tensor elements μ_{mn} and ε_{mn} $((m,n) = (x,z)$, (y,z), (z,x), and $(z,y))$ are set to be zero.

2.1. The TE and TM modes

For the TE mode which is composed of H_z, E_x, and E_y components, the above curl equations can be reduced to

$$\frac{\partial E_y}{\partial x} - \frac{\partial E_x}{\partial y} = -j\omega\mu_0\mu_{zz}H_z \tag{5}$$

$$\frac{\partial H_z}{\partial y} = j\omega\varepsilon_0(\varepsilon_{xx}E_x + \varepsilon_{xy}E_y) \tag{6}$$

$$-\frac{\partial H_z}{\partial x} = j\omega\varepsilon_0(\varepsilon_{yx}E_x + \varepsilon_{yy}E_y). \tag{7}$$

From Eqs. (6) and (7) we can express E_x and E_y in terms of H_z. Substituting these expressions into Eq. (5), we can obtain the governing equation for the TE mode as

$$\frac{\partial}{\partial x}\left(\frac{\varepsilon_{yx}}{\varepsilon_{yx}\varepsilon_{xy} - \varepsilon_{xx}\varepsilon_{yy}}\frac{\partial H_z}{\partial y}\right) + \frac{\partial}{\partial x}\left(\frac{\varepsilon_{xx}}{\varepsilon_{yx}\varepsilon_{xy} - \varepsilon_{xx}\varepsilon_{yy}}\frac{\partial H_z}{\partial x}\right)$$
$$-\frac{\partial}{\partial y}\left(\frac{\varepsilon_{yy}}{\varepsilon_{yy}\varepsilon_{xx} - \varepsilon_{xy}\varepsilon_{yx}}\frac{\partial H_z}{\partial y}\right) - \frac{\partial}{\partial y}\left(\frac{\varepsilon_{xy}}{\varepsilon_{yy}\varepsilon_{xx} - \varepsilon_{xy}\varepsilon_{yx}}\frac{\partial H_z}{\partial x}\right) = k_0^2\mu_{zz}H_z \tag{8}$$

#79272 - $15.00 USD Received 22 Jan 2007; revised 14 Apr 2007; accepted 17 Apr 2007; published 19 Apr 2007

where $k_0 = \omega\sqrt{\mu_0\varepsilon_0}$ is the wave vector in free space.

A similar procedure can be applied to the TM mode. For the TM mode comprising E_z, H_x, and H_y components, Maxwell's curl equations can be simplified to

$$\frac{\partial E_z}{\partial y} = -j\omega\mu_0(\mu_{xx}H_x + \mu_{xy}H_y) \tag{9}$$

$$-\frac{\partial E_z}{\partial x} = -j\omega\mu_0(\mu_{yx}H_x + \mu_{yy}H_y) \tag{10}$$

$$\frac{\partial H_y}{\partial x} - \frac{\partial H_x}{\partial y} = j\omega\varepsilon_0\varepsilon_{zz}E_z. \tag{11}$$

From Eqs. (9) and (10) we can express H_x and H_y in terms of E_z. Substituting these expressions into Eq. (11), again we achieve the governing equation for the TM mode as

$$\begin{aligned}&\frac{\partial}{\partial x}\left(\frac{\mu_{yx}}{\mu_{yx}\mu_{xy}-\mu_{xx}\mu_{yy}}\frac{\partial E_z}{\partial y}\right)+\frac{\partial}{\partial x}\left(\frac{\mu_{xx}}{\mu_{yx}\mu_{xy}-\mu_{xx}\mu_{yy}}\frac{\partial E_z}{\partial x}\right)\\&-\frac{\partial}{\partial y}\left(\frac{\mu_{yy}}{\mu_{yy}\mu_{xx}-\mu_{xy}\mu_{yx}}\frac{\partial E_z}{\partial y}\right)-\frac{\partial}{\partial y}\left(\frac{\mu_{xy}}{\mu_{yy}\mu_{xx}-\mu_{xy}\mu_{yx}}\frac{\partial E_z}{\partial x}\right)=k_0^2\varepsilon_{zz}E_z.\end{aligned} \tag{12}$$

For clarity we can express Eqs. (8) and (12) together in a concise equation as

$$\begin{aligned}&\frac{\partial}{\partial x}\left(\frac{p_{yx}}{p_{yx}p_{xy}-p_{xx}p_{yy}}\frac{\partial \phi_z}{\partial y}\right)+\frac{\partial}{\partial x}\left(\frac{p_{xx}}{p_{yx}p_{xy}-p_{xx}p_{yy}}\frac{\partial \phi_z}{\partial x}\right)\\&-\frac{\partial}{\partial y}\left(\frac{p_{yy}}{p_{yy}p_{xx}-p_{xy}p_{yx}}\frac{\partial \phi_z}{\partial y}\right)-\frac{\partial}{\partial y}\left(\frac{p_{xy}}{p_{yy}p_{xx}-p_{xy}p_{yx}}\frac{\partial \phi_z}{\partial x}\right)=k_0^2 q_{zz}\phi_z\end{aligned} \tag{13}$$

where

$$[p] = \begin{bmatrix} p_{xx} & p_{xy} & p_{xz} \\ p_{yx} & p_{yy} & p_{yz} \\ p_{zx} & p_{zy} & p_{zz} \end{bmatrix} = \begin{bmatrix} \varepsilon_{xx} & \varepsilon_{xy} & 0 \\ \varepsilon_{yx} & \varepsilon_{yy} & 0 \\ 0 & 0 & \varepsilon_{zz} \end{bmatrix} \tag{14}$$

$$[q] = \begin{bmatrix} q_{xx} & q_{xy} & q_{xz} \\ q_{yx} & q_{yy} & q_{yz} \\ q_{zx} & q_{zy} & q_{zz} \end{bmatrix} = \begin{bmatrix} \mu_{xx} & \mu_{xy} & 0 \\ \mu_{yx} & \mu_{yy} & 0 \\ 0 & 0 & \mu_{zz} \end{bmatrix} \tag{15}$$

for the TE mode ($\phi_z = H_z$) and

$$[p] = \begin{bmatrix} p_{xx} & p_{xy} & p_{xz} \\ p_{yx} & p_{yy} & p_{yz} \\ p_{zx} & p_{zy} & p_{zz} \end{bmatrix} = \begin{bmatrix} \mu_{xx} & \mu_{xy} & 0 \\ \mu_{yx} & \mu_{yy} & 0 \\ 0 & 0 & \mu_{zz} \end{bmatrix} \tag{16}$$

$$[q] = \begin{bmatrix} q_{xx} & q_{xy} & q_{xz} \\ q_{yx} & q_{yy} & q_{yz} \\ q_{zx} & q_{zy} & q_{zz} \end{bmatrix} = \begin{bmatrix} \varepsilon_{xx} & \varepsilon_{xy} & 0 \\ \varepsilon_{yx} & \varepsilon_{yy} & 0 \\ 0 & 0 & \varepsilon_{zz} \end{bmatrix} \tag{17}$$

for the TM mode ($\phi_z = E_z$). Note that Eq. (13) applies to both magnetic and dielectric materials with non-diagonal permeability and permittivity tensors provided that the TE and TM modes are decoupled.

2.2. Finite element discretization

For the scalar EM fields, H_z or E_z in Eq. (13), the quadratic triangular element [16,17] with six variables ϕ_{z1}–ϕ_{z6}, one at each of its three vertices and the other three at the middles of its three

#79272 - $15.00 USD Received 22 Jan 2007; revised 14 Apr 2007; accepted 17 Apr 2007; published 19 Apr 2007

sides, as shown in Fig. 1(a), is extremely suitable for the discretization of the FEM. Moreover, in order to improve the accuracy and efficiency in the analysis, the curvilinear counterpart of Fig. 1(a), depicted in Fig. 1(b), is preferred and is adopted in our FEM based eigenvalue algorithm. The six shape functions of the quadratic triangular element are given by

$$\{N\} = \begin{bmatrix} N_1 \\ N_2 \\ N_3 \\ N_4 \\ N_5 \\ N_6 \end{bmatrix} = \begin{bmatrix} L_1(2L_1-1) \\ L_2(2L_2-1) \\ L_3(2L_3-1) \\ 4L_1L_2 \\ 4L_2L_3 \\ 4L_3L_1 \end{bmatrix} \tag{18}$$

provided that the nodes are numbered as shown in Fig. 1(a). In Eq. (18), L_i ($i = 1,2,3$) are the simplex coordinates defined as

$$L_i = \frac{1}{2\Delta}(a_i + b_i x + c_i y) \tag{19}$$

with

$$a_i = x_{i+1}y_{i+2} - x_{i+2}y_{i+1} \tag{20}$$

$$b_i = y_{i+1} - y_{i-1} \tag{21}$$

$$c_i = x_{i-1} - x_{i+1} \tag{22}$$

where x_i and y_i are the Cartesian coordinates of the ith vertex and Δ represents the area of the triangular element, that is,

$$\Delta = \left|\frac{1}{2}(a_1 + a_2 + a_3)\right| = \left|\frac{1}{2}(b_{i+1}c_{i-1} - b_{i-1}c_{i+1})\right|. \tag{23}$$

Here the index i in Eqs. (20)–(23) assumes values $1,2,3$, cyclically, so that if $i = 3$, then $i+1 = 1$.

In the curvilinear element, the Cartesian coordinates, x and y, can be approximated as

$$x = \sum_{j=1}^{6} N_j x_j \tag{24}$$

$$y = \sum_{j=1}^{6} N_j y_j \tag{25}$$

where x_j and y_j are the Cartesian coordinates of the jth node ($j =$ 1–6) within each element and N_i is defined in Eq. (18). Noting that $L_1 + L_2 + L_3 = 1$ and selecting L_1 and L_2 as the independent variables, the relation of differentiation between the Cartesian coordinate system and the simplex coordinate system can be written as

$$\begin{bmatrix} \dfrac{\partial}{\partial L_1} \\ \dfrac{\partial}{\partial L_2} \end{bmatrix} = [J] \begin{bmatrix} \dfrac{\partial}{\partial x} \\ \dfrac{\partial}{\partial y} \end{bmatrix} \tag{26}$$

where $[J]$ is the Jacobian matrix of the transformation given by

$$[J] = \begin{bmatrix} \dfrac{\partial x}{\partial L_1} & \dfrac{\partial y}{\partial L_1} \\ \dfrac{\partial x}{\partial L_2} & \dfrac{\partial y}{\partial L_2} \end{bmatrix}. \tag{27}$$

#79272 - $15.00 USD Received 22 Jan 2007; revised 14 Apr 2007; accepted 17 Apr 2007; published 19 Apr 2007

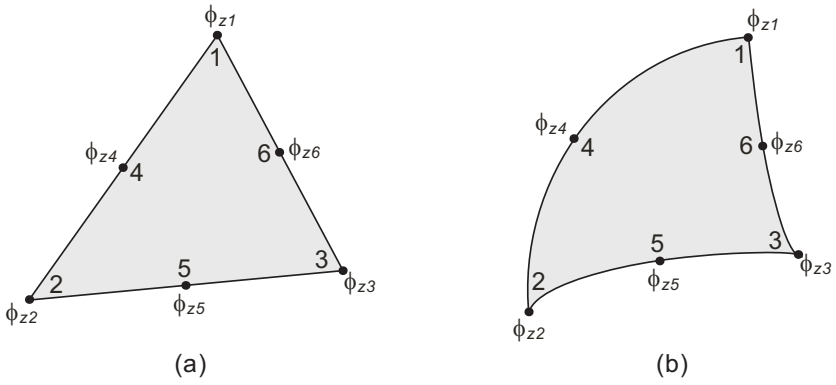

Fig. 1. (a) Quadratic triangular element. (b) Curvilinear triangular element.

Moreover, the integration of a function $f(x,y)$ in the Cartesian coordinate system can be performed in the simplex coordinate system through

$$\int\int_e f(x,y)dxdy = \int_0^1 \left[\int_0^{1-L_1} f(L_1,L_2,L_3)\,|J(L_1,L_2,L_3)|\,dL_2 \right] dL_1 \tag{28}$$

where $|J|$ is the Jacobian, the determinant of $[J]$. Hence, the required computation for element matrices associated with the governing equation can be obtained directly in the simplex coordinate system.

Dividing the structure domain into a number of curvilinear triangular elements, the field ϕ_z in each element can be expanded as $\phi_z = \{N\}^T\{\phi_z^e\}$, where $\{\phi_z^e\}$ is the variable vector for each element, and T denotes transpose. Applying Galerkin's method and assembling all element matrices, Eq. (13) can be transformed into the matrix form as

$$[K]\{\phi_z\} - k_0^2[M]\{\phi_z\} = \{\psi\} \tag{29}$$

with

$$\begin{aligned}[K] = \sum_e \int\int \Bigg(& -\frac{p_{yx}}{p_{yx}p_{xy}-p_{xx}p_{yy}} \frac{\partial\{N\}}{\partial x}\frac{\partial\{N\}^T}{\partial y} - \frac{p_{xx}}{p_{yx}p_{xy}-p_{xx}p_{yy}} \frac{\partial\{N\}}{\partial x}\frac{\partial\{N\}^T}{\partial x} \\ & + \frac{p_{yy}}{p_{yy}p_{xx}-p_{xy}p_{yx}} \frac{\partial\{N\}}{\partial y}\frac{\partial\{N\}^T}{\partial y} + \frac{p_{xy}}{p_{yy}p_{xx}-p_{xy}p_{yx}} \frac{\partial\{N\}}{\partial y}\frac{\partial\{N\}^T}{\partial x} \Bigg) dxdy \end{aligned} \tag{30}$$

$$[M] = \sum_e \int\int \left(q_{zz}\{N\}\{N\}^T\right) dxdy \tag{31}$$

$$\begin{aligned}\{\psi\} = \sum_e \int \Bigg[& \hat{x}\left(-\frac{p_{yx}}{p_{yx}p_{xy}-p_{xx}p_{yy}}\{N\}\frac{\partial\phi_z}{\partial y} - \frac{p_{xx}}{p_{yx}p_{xy}-p_{xx}p_{yy}}\{N\}\frac{\partial\phi_z}{\partial x} \right) \\ & + \hat{y}\left(\frac{p_{yy}}{p_{yy}p_{xx}-p_{xy}p_{yx}}\{N\}\frac{\partial\phi_z}{\partial y} + \frac{p_{xy}}{p_{yy}p_{xx}-p_{xy}p_{yx}}\{N\}\frac{\partial\phi_z}{\partial x} \right) \Bigg] \cdot \hat{n}dl \end{aligned} \tag{32}$$

where l denotes the contour or boundary enclosing the area, $\hat{n}$ is its outward normal vector, and $\sum_e$ extends over all different elements. Note that Eq. (29) is not an eigenvalue matrix equation due to the existence of the vector $\{\psi\}$ on the right-hand side. Fortunately, this term can be eliminated as a consequence of imposing the PBCs in our numerical model, as will be described in the next subsection.

#79272 - $15.00 USD Received 22 Jan 2007; revised 14 Apr 2007; accepted 17 Apr 2007; published 19 Apr 2007

2.3. *Periodic boundary conditions for the 2D PCs*

Due to the periodicity, PCs can be entirely described by the concept of unit cell along with the PBCs. Therefore, the correct setting of PBCs in the numerical model is extremely important. For a square unit cell, with the four sides labeled by I, II, III, and IV, respectively, as shown in Fig. 2(a), the PBCs can be expressed as

$$\phi_z|_{\mathrm{I}} = e^{-jk_x a}\phi_z|_{\mathrm{III}} \tag{33}$$

$$\frac{\partial \phi_z}{\partial x}\Big|_{\mathrm{I}} = e^{-jk_x a}\frac{\partial \phi_z}{\partial x}\Big|_{\mathrm{III}} \tag{34}$$

$$\frac{\partial \phi_z}{\partial y}\Big|_{\mathrm{I}} = e^{-jk_x a}\frac{\partial \phi_z}{\partial y}\Big|_{\mathrm{III}} \tag{35}$$

$$\phi_z|_{\mathrm{II}} = e^{-jk_y a}\phi_z|_{\mathrm{IV}} \tag{36}$$

$$\frac{\partial \phi_z}{\partial x}\Big|_{\mathrm{II}} = e^{-jk_y a}\frac{\partial \phi_z}{\partial x}\Big|_{\mathrm{IV}} \tag{37}$$

$$\frac{\partial \phi_z}{\partial y}\Big|_{\mathrm{II}} = e^{-jk_y a}\frac{\partial \phi_z}{\partial y}\Big|_{\mathrm{IV}} \tag{38}$$

where k_x and k_y are the wavenumbers in the x and y directions, respectively, and a is the lattice distance. To adequately incorporate these conditions into the numerical model, the whole boundary is grouped into three parts, as depicted in Fig. 2(a). The fields at the two vertical sides are connected by Eqs. (33)–(35), whereas those at the two horizontal sides are related by Eqs. (36)–(38). To demonstrate the application of Eqs. (33)–(38) concretely, the elements in vectors $\{\phi_z\}$ and $\{\psi\}$ in Eq. (29) are classified first according to the locations of the corresponding variables and Eq. (29) can be rewritten in the following form

$$\begin{bmatrix} [K]_{11} & [K]_{12} & [K]_{13} & [K]_{14} & [K]_{15} \\ [K]_{21} & [K]_{22} & [K]_{23} & [K]_{24} & [K]_{25} \\ [K]_{31} & [K]_{32} & [K]_{33} & [K]_{34} & [K]_{35} \\ [K]_{41} & [K]_{42} & [K]_{43} & [K]_{44} & [K]_{45} \\ [K]_{51} & [K]_{52} & [K]_{53} & [K]_{54} & [K]_{55} \end{bmatrix} \begin{bmatrix} \{\phi_z\}_0 \\ \{\phi_z\}_{\mathrm{I}} \\ \{\phi_z\}_{\mathrm{II}} \\ \{\phi_z\}_{\mathrm{III}} \\ \{\phi_z\}_{\mathrm{IV}} \end{bmatrix}$$
$$-k_0^2 \begin{bmatrix} [M]_{11} & [M]_{12} & [M]_{13} & [M]_{14} & [M]_{15} \\ [M]_{21} & [M]_{22} & [M]_{23} & [M]_{24} & [M]_{25} \\ [M]_{31} & [M]_{32} & [M]_{33} & [M]_{34} & [M]_{35} \\ [M]_{41} & [M]_{42} & [M]_{43} & [M]_{44} & [M]_{45} \\ [M]_{51} & [M]_{52} & [M]_{53} & [M]_{54} & [M]_{55} \end{bmatrix} \begin{bmatrix} \{\phi_z\}_0 \\ \{\phi_z\}_{\mathrm{I}} \\ \{\phi_z\}_{\mathrm{II}} \\ \{\phi_z\}_{\mathrm{III}} \\ \{\phi_z\}_{\mathrm{IV}} \end{bmatrix} = \begin{bmatrix} \{0\} \\ \{\psi\}_{\mathrm{I}} \\ \{\psi\}_{\mathrm{II}} \\ \{\psi\}_{\mathrm{III}} \\ \{\psi\}_{\mathrm{IV}} \end{bmatrix} \tag{39}$$

where $\{\phi_z\}_0$ stands for the vector of variables in the interior region, the subscripts, I, II, III, and IV, denote the sides at which the variables locate, and

$$\{\psi\}_{\mathrm{I}} = \sum_e \int \left(-\frac{p_{yx}}{p_{yx}p_{xy} - p_{xx}p_{yy}}\{N\}\frac{\partial \phi_z}{\partial y}\Big|_{\mathrm{I}} - \frac{p_{xx}}{p_{yx}p_{xy} - p_{xx}p_{yy}}\{N\}\frac{\partial \phi_z}{\partial x}\Big|_{\mathrm{I}} \right) dl \tag{40}$$

$$\{\psi\}_{\mathrm{II}} = \sum_e \int \left(\frac{p_{yy}}{p_{yy}p_{xx} - p_{xy}p_{yx}}\{N\}\frac{\partial \phi_z}{\partial y}\Big|_{\mathrm{II}} + \frac{p_{xy}}{p_{yy}p_{xx} - p_{xy}p_{yx}}\{N\}\frac{\partial \phi_z}{\partial x}\Big|_{\mathrm{II}} \right) dl \tag{41}$$

$$\{\psi\}_{\mathrm{III}} = \sum_e \int \left(\frac{p_{yx}}{p_{yx}p_{xy} - p_{xx}p_{yy}}\{N\}\frac{\partial \phi_z}{\partial y}\Big|_{\mathrm{III}} + \frac{p_{xx}}{p_{yx}p_{xy} - p_{xx}p_{yy}}\{N\}\frac{\partial \phi_z}{\partial x}\Big|_{\mathrm{III}} \right) dl \tag{42}$$

$$\{\psi\}_{\mathrm{IV}} = \sum_e \int \left(-\frac{p_{yy}}{p_{yy}p_{xx} - p_{xy}p_{yx}}\{N\}\frac{\partial \phi_z}{\partial y}\Big|_{\mathrm{IV}} - \frac{p_{xy}}{p_{yy}p_{xx} - p_{xy}p_{yx}}\{N\}\frac{\partial \phi_z}{\partial x}\Big|_{\mathrm{IV}} \right) dl. \tag{43}$$

#79272 - $15.00 USD Received 22 Jan 2007; revised 14 Apr 2007; accepted 17 Apr 2007; published 19 Apr 2007

Note that columns 2 and 4 as well as columns 3 and 5 of matrices $[K]$ and $[M]$ in Eq. (39) can be combined through Eqs. (33) and (36), respectively. Furthermore, if we divide row 2 in Eq. (39) by e^{-jk_xa} and add it to row 4, $\{\psi\}_{\rm I}$ and $\{\psi\}_{\rm III}$ will cancel each other by the use of Eqs. (34) and (35). Similarly, $\{\psi\}_{\rm II}$ and $\{\psi\}_{\rm IV}$ can cancel each other when row 3 in Eq. (39) is divided by e^{-jk_ya} and then added to row 5 with the help of Eqs. (37) and (38). By means of these operations, Eq. (39) becomes

$$\begin{bmatrix} [K]_{11} & [K]_{14}+e^{-jk_xa}[K]_{12} & [K]_{15}+e^{-jk_ya}[K]_{13} \\ [K]_{41}+\frac{1}{e^{-jk_xa}}[K]_{21} & [K]_{44}+e^{-jk_xa}[K]_{42}+\frac{1}{e^{-jk_xa}}([K]_{24}+e^{-jk_xa}[K]_{22}) & [K]_{45}+e^{-jk_ya}[K]_{43}+\frac{1}{e^{-jk_xa}}([K]_{25}+e^{-jk_ya}[K]_{23}) \\ [K]_{51}+\frac{1}{e^{-jk_ya}}[K]_{31} & [K]_{54}+e^{-jk_xa}[K]_{52}+\frac{1}{e^{-jk_ya}}([K]_{34}+e^{-jk_xa}[K]_{32}) & [K]_{55}+e^{-jk_ya}[K]_{53}+\frac{1}{e^{-jk_ya}}([K]_{35}+e^{-jk_ya}[K]_{33}) \end{bmatrix} \begin{bmatrix} \{\phi_z\}_0 \\ \{\phi_z\}_{\rm III} \\ \{\phi_z\}_{\rm IV} \end{bmatrix}$$
$$-k_0^2 \begin{bmatrix} [M]_{11} & [M]_{14}+e^{-jk_xa}[M]_{12} & [M]_{15}+e^{-jk_ya}[M]_{13} \\ [M]_{41}+\frac{1}{e^{-jk_xa}}[M]_{21} & [M]_{44}+e^{-jk_xa}[M]_{42}+\frac{1}{e^{-jk_xa}}([M]_{24}+e^{-jk_xa}[M]_{22}) & [M]_{45}+e^{-jk_ya}[M]_{43}+\frac{1}{e^{-jk_xa}}([M]_{25}+e^{-jk_ya}[M]_{23}) \\ [M]_{51}+\frac{1}{e^{-jk_ya}}[M]_{31} & [M]_{54}+e^{-jk_xa}[M]_{52}+\frac{1}{e^{-jk_ya}}([M]_{34}+e^{-jk_xa}[M]_{32}) & [M]_{55}+e^{-jk_ya}[M]_{53}+\frac{1}{e^{-jk_ya}}([M]_{35}+e^{-jk_ya}[M]_{33}) \end{bmatrix} \begin{bmatrix} \{\phi_z\}_0 \\ \{\phi_z\}_{\rm III} \\ \{\phi_z\}_{\rm IV} \end{bmatrix} = \begin{bmatrix} \{0\} \\ \{0\} \\ \{0\} \end{bmatrix}. \quad (44)$$

Through this procedure, the information at sides I and II is conveniently associated with that at sides III and IV, and the matrices and vectors in Eq. (29) are correctly modified to obtain the desired eigenvalue matrix equation of Eq. (44). Please note that, as every vertex belongs to a vertical and a horizontal side simultaneously, it is proper that the fields at the four vertices are linked together by the use of Eqs. (33)–(38), as has been automatically included in the above manipulation of Eq. (29). This idea is indicated by the arrows in Fig. 2(a).

As for a hexagonal unit cell, the PBCs can be written as

$$\phi_z|_{\rm I} = e^{-j(k_x\frac{\sqrt{3}a}{2}+k_y\frac{a}{2})}\phi_z|_{\rm IV} \quad (45)$$
$$\frac{\partial\phi_z}{\partial x}\Big|_{\rm I} = e^{-j(k_x\frac{\sqrt{3}a}{2}+k_y\frac{a}{2})}\frac{\partial\phi_z}{\partial x}\Big|_{\rm IV} \quad (46)$$
$$\frac{\partial\phi_z}{\partial y}\Big|_{\rm I} = e^{-j(k_x\frac{\sqrt{3}a}{2}+k_y\frac{a}{2})}\frac{\partial\phi_z}{\partial y}\Big|_{\rm IV} \quad (47)$$
$$\phi_z|_{\rm II} = e^{-jk_ya}\phi_z|_{\rm V} \quad (48)$$
$$\frac{\partial\phi_z}{\partial x}\Big|_{\rm II} = e^{-jk_ya}\frac{\partial\phi_z}{\partial x}\Big|_{\rm V} \quad (49)$$
$$\frac{\partial\phi_z}{\partial y}\Big|_{\rm II} = e^{-jk_ya}\frac{\partial\phi_z}{\partial y}\Big|_{\rm V} \quad (50)$$
$$\phi_z|_{\rm III} = e^{j(k_x\frac{\sqrt{3}a}{2}-k_y\frac{a}{2})}\phi_z|_{\rm VI} \quad (51)$$
$$\frac{\partial\phi_z}{\partial x}\Big|_{\rm III} = e^{j(k_x\frac{\sqrt{3}a}{2}-k_y\frac{a}{2})}\frac{\partial\phi_z}{\partial x}\Big|_{\rm VI} \quad (52)$$
$$\frac{\partial\phi_z}{\partial y}\Big|_{\rm III} = e^{j(k_x\frac{\sqrt{3}a}{2}-k_y\frac{a}{2})}\frac{\partial\phi_z}{\partial y}\Big|_{\rm VI} \quad (53)$$

provided that the six sides are labeled as shown in Fig. 2(b). The whole boundary of the hexagonal unit cell is grouped into five parts, as implied in Fig. 2(b), for the implementation of the

#79272 - $15.00 USD Received 22 Jan 2007; revised 14 Apr 2007; accepted 17 Apr 2007; published 19 Apr 2007

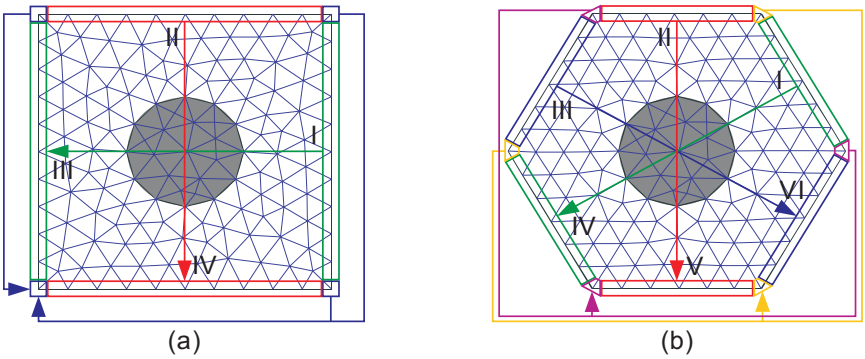

Fig. 2. (a) A square unit cell and its corresponding PBCs. (b) A hexagonal unit cell and its corresponding PBCs.

PBCs. The fields at sides I and IV, II and V, and III and VI are, respectively, connected by Eqs. (45)–(47), (48)–(50), and (51)–(53). Certainly, the six vertices should be considered separately because every vertex has two adjoining boundaries. Examining the relative positions of the six vertices carefully, the six vertices are partitioned into two independent parts, in each of which any vertex is at a distance a from the other two vertices. In each part, the fields at the three vertices can be linked together using Eqs. (45)–(53). The arrows in Fig. 2(b) illustrate this idea. Same as in the case of square unit cell, associating the information at sides I, II, and III with that at sides IV, V, and VI, respectively, will suitably modify the matrices and vectors in Eq. (29), and consequently the desired eigenvalue matrix equation can be derived.

3. Numerical results

For the analysis and discussion, we consider two 2D PCs formed by square- and triangle-arranged parallel silicon rods surrounded by nematic LCs (5CB) [18]. We choose the LCs as our anisotropic material for the convenient change of anisotropy by simply rotating the LC molecules. The components of the relative permittivity tensor $[\varepsilon_r]$ of the nematic LCs we use are given as

$$\varepsilon_{xx} = n_o^2 + (n_e^2 - n_o^2)\sin^2\theta_c \cos^2\phi_c \tag{54}$$

$$\varepsilon_{xy} = \varepsilon_{yx} = (n_e^2 - n_o^2)\sin^2\theta_c \sin\phi_c \cos\phi_c \tag{55}$$

$$\varepsilon_{xz} = \varepsilon_{zx} = (n_e^2 - n_o^2)\sin\theta_c \cos\theta_c \cos\phi_c \tag{56}$$

$$\varepsilon_{yy} = n_o^2 + (n_e^2 - n_o^2)\sin^2\theta_c \sin^2\phi_c \tag{57}$$

$$\varepsilon_{yz} = \varepsilon_{zy} = (n_e^2 - n_o^2)\sin\theta_c \cos\theta_c \sin\phi_c \tag{58}$$

$$\varepsilon_{zz} = n_o^2 + (n_e^2 - n_o^2)\cos^2\theta_c \tag{59}$$

where $n_o = 1.5292$ and $n_e = 1.7072$ are, respectively, the ordinary and extraordinary refractive indices of the nematic LCs, θ_c is the angle between the crystal c-axis and the z-axis, and ϕ_c represents the angle between the projection of the crystal c-axis on the x-y plane and the x-axis, as defined in Fig. 3. For the decoupling of the TE and TM modes in the 2D condition. The angle, θ_c, is set to be 90° and thus the LC molecules will merely rotate in the x-y plane.

The band structures of these two kinds of lattices will be separately analyzed in the next two subsections. For the TM mode, the electric field only possesses z-component and will regard the anisotropic PC as an isotropic one. So we will focus our discussion on the band structures

#79272 - $15.00 USD Received 22 Jan 2007; revised 14 Apr 2007; accepted 17 Apr 2007; published 19 Apr 2007

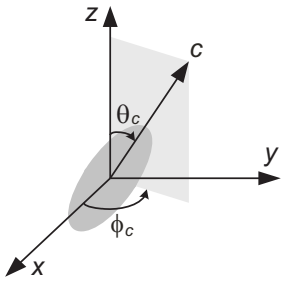

Fig. 3. Schematic definition of rotation angles for the LC molecule.

of the TE mode. From the numerical results we will explain the concept of constructing the band structures for anisotropic PCs clearly.

3.1. Square lattice

The first structure under consideration is the 2D PC with square lattice, as illustrated in Fig. 4(a), consisting of square-arranged parallel silicon rods with relative permittivity $\varepsilon_r = 11.56$ and radius $r = 0.2a$ in the background material of LCs. The unit cell of this structure is also indicated by the square region in Fig. 4(a), and the corresponding first BZ of the reciprocal lattice is depicted in Fig. 4(b). For isotropic PCs, a complete band structure can be conveniently constructed by simply considering all the possible directions of the wave vector **k** restricted in the irreducible BZ (IBZ) which is enclosed by points Γ, X, and M, as shown in Fig. 4(b). The reliability and completeness of the band structure obtained from this IBZ for isotropic PCs are fully based on the structure symmetry, including the rotation and reflection symmetry. For anisotropic PCs, the situation becomes more complicated because the circumstance experienced by the EM waves is highly direction-dependent. The anisotropy may break the structure symmetry, which in isotropic cases can be totally determined by the spatial configuration of materials. With this consideration, it is reasonable to inspect more band structures constructed from different directions of **k** in the first BZ.

To illustrate this phenomenon specifically, we take the square-arranged 2D PC of $\phi_c = 30^\circ$ as an example. We compute the normalized frequencies for four distinct sub-zones in the first BZ marked by Γ-X-M, Γ-X′-M, Γ-X′-M′, and Γ-X″-M′, as indicated in Fig. 4(b), which are absolutely identical to isotropic PCs. The results are depicted in Fig. 5, in which the six possible

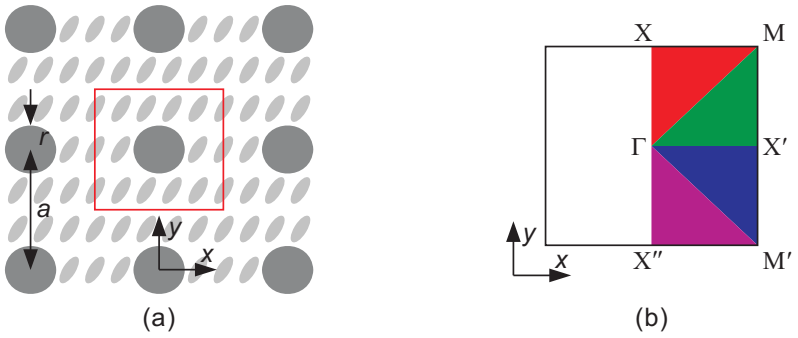

Fig. 4. (a) The cross-section of a 2D PC with square lattice in the background of LCs. (b) The first BZ of (a).

#79272 - $15.00 USD Received 22 Jan 2007; revised 14 Apr 2007; accepted 17 Apr 2007; published 19 Apr 2007

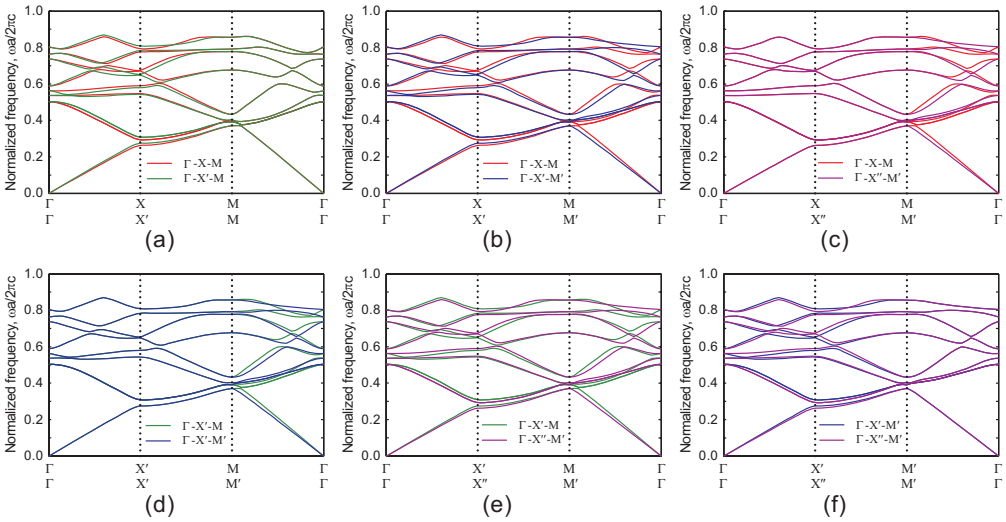

Fig. 5. Comparisons of band structures for the 2D PC with square lattice of $\phi_c = 30^\circ$ between different sub-zones. (a) Γ-X-M and Γ-X′-M; (b) Γ-X-M and Γ-X′-M′; (c) Γ-X-M and Γ-X″-M′; (d) Γ-X′-M and Γ-X′-M′; (e) Γ-X′-M and Γ-X″-M′; (f) Γ-X′-M′ and Γ-X″-M′.

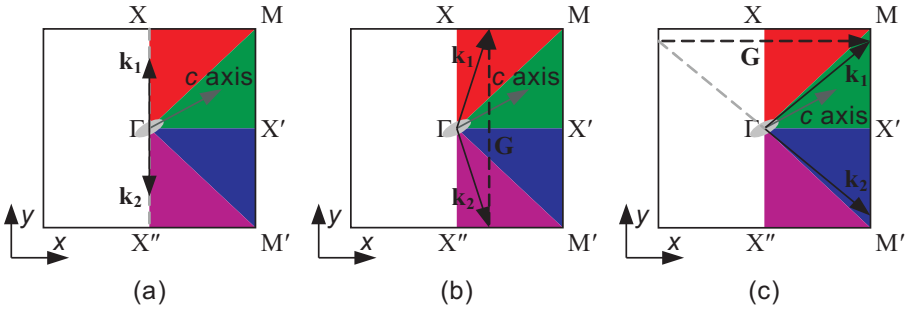

Fig. 6. Explanations for the equivalence of band structures of the 2D PC with square lattice between certain directions of the wave vector in the first BZ.

comparisons for the four sub-zones are carefully examined in turn to figure out the relationships between them. In this figure, we use different colors to distinguish the four band structures obtained from the four distinct sub-zones defined before. In Fig. 5(a), the two band structures from Γ-X-M and Γ-X′-M are dissimilar to each other except for the segment M-Γ. This can be easily understood because the segment M-Γ is shared by Γ-X-M and Γ-X′-M. The consistency of results for segments Γ-X′ and M′-Γ in Fig. 5(d) and (f), respectively, can be explained by this same reason. We then proceed to Fig. 5(c) where we can observe that the two band structures from Γ-X-M and Γ-X″-M′ are exactly the same excluding the third part. The equivalence of the segments Γ-X and Γ-X″ can be visualized by the aid of Fig. 6(a). Although the direction of $\mathbf{k_1}$ along segment Γ-X is opposite to that of $\mathbf{k_2}$ along segment Γ-X″, the rotation symmetry of the structure actually makes waves of these two wave vectors experience alike material property. Thus the band structure from these two segments are identical to each other. The reason for the equivalence of segments X-M and X″-M′ is quite different because now $\mathbf{k_1}$ along segment X-M does not point to the contrary direction of $\mathbf{k_2}$ along segment X″-M′, and it cannot be attributed

#79272 - $15.00 USD Received 22 Jan 2007; revised 14 Apr 2007; accepted 17 Apr 2007; published 19 Apr 2007

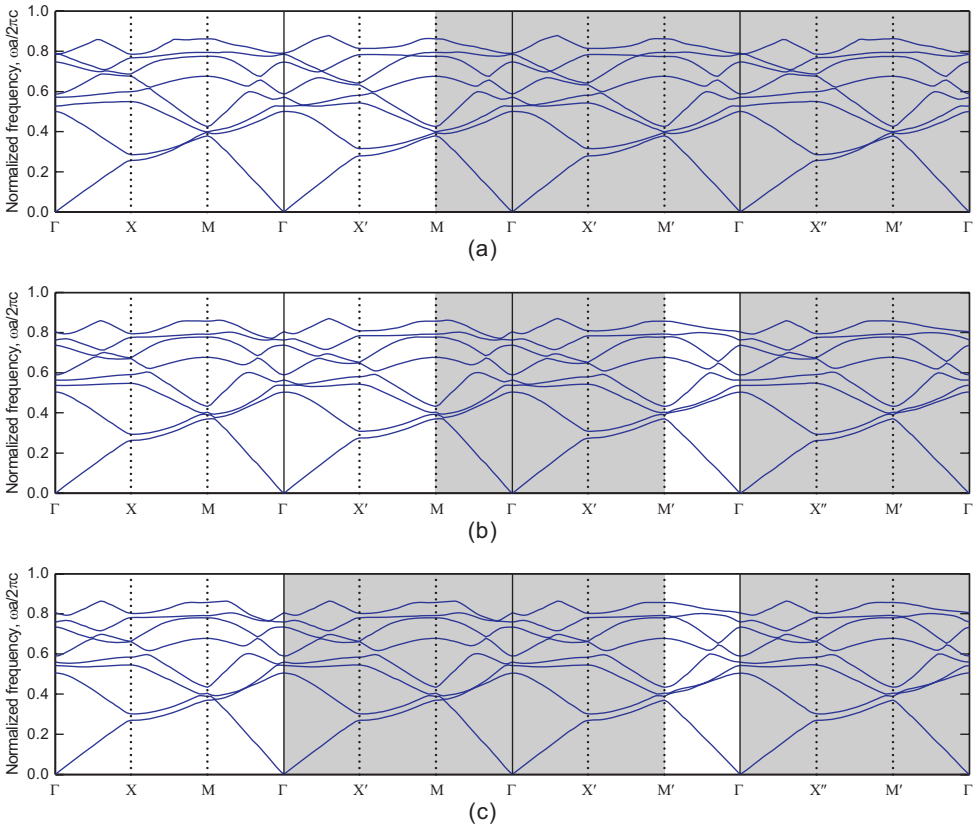

Fig. 7. The band structures of the TE mode for the 2D PC with square lattice of (a) $\phi_c = 0^\circ$, (b) $\phi_c = 30^\circ$, and (c) $\phi_c = 45^\circ$.

to the rotation symmetry. Besides, the appearance of LCs rotating at $\phi_c = 30^\circ$ also prevents the reflection symmetry from a reasonable explanation. To explain what causes the identity of segments X-M and X$''$-M$'$, we appeal to the basic principle of periodic structures. For periodic structures, every lattice vector $\mathbf{R}$ and reciprocal lattice vector $\mathbf{G}$ must satisfy the requirement $\mathbf{G}\cdot\mathbf{R} = 2\pi N$ where N is an integer [3]. Thus if $\mathbf{k}$ is incremented by $\mathbf{G}$, the phase between cells is incremented by $\mathbf{G}\cdot\mathbf{R}$, which is equal to $2\pi N$ and does not really affect the mode. For every pair of wave vectors, $\mathbf{k_1}$ and $\mathbf{k_2}$, of segments X-M and X$''$-M$'$, the difference between them is exactly a reciprocal lattice vector $\mathbf{G}$, as depicted in Fig. 6(b), so it is no surprise that the band structures of these two segments are the same. Next we examine segments X$'$-M and X$'$-M$'$, another identical pair as shown in Fig. 5(d). The identity of this pair can be reasonably accepted by applying the two reasons just mentioned above simultaneously. This idea is illustrated in Fig. 6(c) which reveals that the difference between $\mathbf{k_1}$ and $\mathbf{k_2}$ is also exactly $\mathbf{G}$. In Fig. 5(b) and (e), no conditions mentioned above occur, and, consequently, the whole band structures from these corresponding sub-zones are quite unlike.

When the LC molecules rotate to $\phi_c = 45^\circ$, another interesting behavior of the band structure can be observed. With LC molecules orienting to this special direction, the resultant structure, determined by the arrangement of silicon rods and the orientation of LC molecules, has reflection symmetry about the c-axis of LCs. According to this observation, it is absolutely reasonable to predict that the band structures from Γ-X-M and Γ-X$'$-M$'$ are identical to those from Γ-X$'$-M

#79272 - $15.00 USD Received 22 Jan 2007; revised 14 Apr 2007; accepted 17 Apr 2007; published 19 Apr 2007

and Γ-X′′-M′, respectively. The reflection symmetry of structures will vary with the rotation angle of LC molecules, but the primary idea discussed above works well and can be considered as a general principle applied to any anisotropic PCs.

We have demonstrated the possible relationships among the four distinct sub-zones in the first BZ clearly and comprehended that there really exists discrepancy among these sub-zones for anisotropic PCs. Consequently, to correctly construct the complete band structures of anisotropic PCs with square lattice, all the independent segments in these four distinct sub-zones should be considered collectively. We show the band structures of the TE mode for this anisotropic PC with square lattice of $\phi_c = 0^\circ$, 30°, and 45° in Fig. 7 from which we can see that there are no photonic band gaps for these different LC rotation angles. Notice that these band structures are constructed from the four sub-zones and the shadowed regions represent ignorable parts because they can be duplicated from unshadowed parts.

3.2. Triangular lattice

Fig. 8(a) shows the cross-section of the second structure to be analyzed, the 2D anisotropic PC with triangular lattice. Except for the lattice configuration, the structure parameters are the same as those of the square-arranged case. The unit cell for this 2D PC is a hexagon as indicated in Fig. 8(a) and the corresponding first BZ of the reciprocal lattice is also a hexagon, as plotted in Fig. 8(b). The analysis of band structures for this PC with triangular lattice is similar to that with square lattice discussed in the last subsection. For a hexagonal BZ, it is necessary to consider the six distinct sub-zones as marked in Fig. 8(b) for obtaining the complete band structures. The understanding about possible relationships among these six sub-zones can be conveniently accomplished in an analogous way as in the square BZ case.

We show the band structures of the TE mode for this PC of $\phi_c = 0^\circ, 30^\circ$, and 45° in Fig. 9. To get an insight into the effect of the anisotropic material on the band gap, we concentrate on Fig. 9(a), the case of $\phi_c = 0^\circ$, first. The red region, if exists, in every one of the six distinct sub-zones stands for the band gap of the structure found from the corresponding sub-zone. For $\phi_c = 0^\circ$, Γ-M-K, Γ-M-K′, and Γ-M′-K′ are identical to Γ-M′′-K′′′, Γ-M′′-K′′, and Γ-M′-K′′, respectively. Accordingly, it is obvious that the band gaps corresponding to these respective pairs are exactly the same to each other. The main point worth emphasizing here is that the normalized frequencies between which the band gaps exist for Γ-M-K, Γ-M-K′, and Γ-M′-K′ are different. So to describe the band gap of this structure suitably, we should find the normalized frequency range appearing simultaneously in all distinct band gaps. Then this normalized frequent range will stand for the correct band gap of the structure. Specifically, the band gap found from Γ-M-K falls between the normalized frequencies of 0.636 and 0.656, whereas the

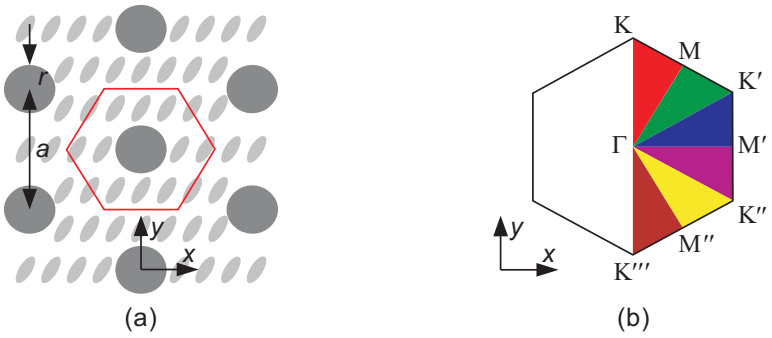

Fig. 8. (a) The cross-section of a 2D PC with triangular lattice in the background of LCs. (b) The first BZ of (a).

#79272 - $15.00 USD Received 22 Jan 2007; revised 14 Apr 2007; accepted 17 Apr 2007; published 19 Apr 2007

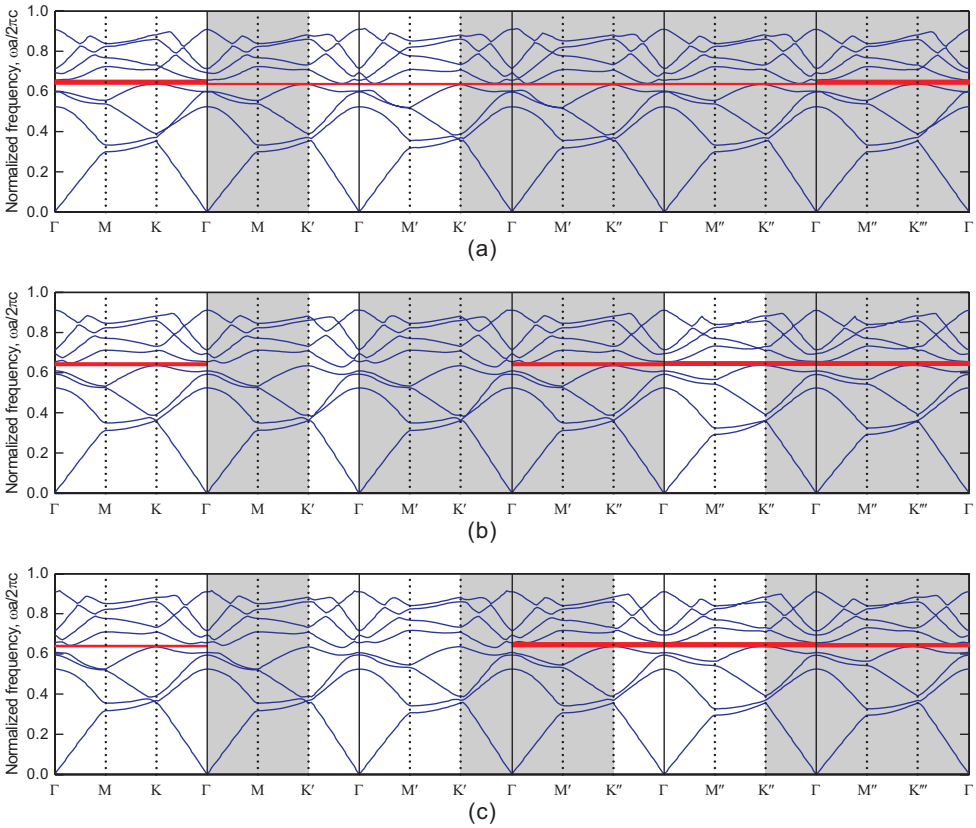

Fig. 9. The band structures of the TE mode for the 2D PC with triangular lattice of (a) $\phi_c = 0^\circ$, (b) $\phi_c = 30^\circ$, and (c) $\phi_c = 45^\circ$.

two numbers obtained from Γ-M-K′ and Γ-M′-K′ are, respectively, 0.635 and 0.640, and 0.634 and 0.639. As a result, the correct band gap of this PC for $\phi_c = 0^\circ$ will exist when the normalized frequency falls between 0.636 and 0.639. In Fig. 9(b) and (c), there are two parts, obtained from Γ-M-K′ and Γ-M′-K′, that do not have band gaps, and hence there do not exist band gaps at all directions for $\phi_c = 30^\circ$ and $\phi_c = 45^\circ$. With these examples, we can see that the anisotropy indeed has a great effect on the behavior of band structures and should be taken into account for constructing a complete band structure.

4. Conclusion

We have successfully developed an FEM based eigenvalue algorithm for analyzing the band structures of 2D anisotropic PCs when the TE and TM modes are decoupled. To demonstrate this algorithm, two 2D anisotropic PCs, the square- and triangle-arranged lattices composed of parallel silicon rods and nematic LCs, are analyzed. The relationships among the distinct sub-zones of the first BZs for these two structures are examined carefully. The concept of constructing complete band structures for isotropic PCs considering only the IBZ should be modified for anisotropic PCs by taking into accounts enough necessary sub-zones in the BZ to ensure the correctness and completeness of band structures. In closing, we like to remark that we have also developed a more general FDFD based eigenvalue algorithm that can treat the PCs discussed here and the numerical results presented in this paper completely agree with those

#79272 - $15.00 USD Received 22 Jan 2007; revised 14 Apr 2007; accepted 17 Apr 2007; published 19 Apr 2007

computed by the FDFD algorithm. Such agreement confirms the correctness of the present analysis. The FDFD work will be published elsewhere.

Acknowledgments

This work was supported in part by the National Science Council of the Republic of China under grant NSC95-2221-E-002-328, in part by the Ministry of Economic Affairs of the Republic of China under grant 95-EC-17-A-08-S1-0006, in part by the Excellent Research Projects of National Taiwan University under grant 95R0062-AE00-06, and in part by the Ministry of Education of the Republic of China under "The Aim of Top University Plan" grant.

#79272 - $15.00 USD Received 22 Jan 2007; revised 14 Apr 2007; accepted 17 Apr 2007; published 19 Apr 2007

Appendix II

A finite-element imaginary-time beam propagation method for two-dimensional photonic crystal analysis

Sen-ming Hsu, Bang-yan Lin, and Hung-chun Chang
Graduate Institute of Photonics and Optoelectronics, Graduate Institute of Communication Engineering, and Department of Electrical Engineering,
National Taiwan University, Taipei, Taiwan 106-17, R.O.C.
Phone: +886-2-23635251-513 Fax: +886-2-23683824 E-mail: hcchang@cc.ee.ntu.edu.tw

Abstract — *A finite-element imaginary-time beam propagation method is developed for the band structure analysis of two-dimensional photonic crystals. The correctness of this scheme is verified by the analysis of a square-arranged photonic crystal.*

Introduction

The imaginary-distance beam propagation method (ID-BPM) is often used for the eigenmode analysis in longitudinally invariant optical waveguides [1,2]. In the ID-BPM, the propagation direction is selected along a spatial imaginary axis, and the specific eigenmode can be extracted from the initial input field by choosing the appropriate propagation step size. Following this idea, we try to develop an imaginary-time beam propagation method (IT-BPM) for the analysis of band structures of two-dimensional (2D) photonic crystals (PCs). To obtain the eigen-frequency of every mode for the construction of the band structure, the propagation direction is selected along a temporal imaginary axis. Then the appropriate propagation time step size is determined in a similar way as in the determination of the propagation step size in the ID-BPM for extracting the specific eigenmode from the initial input field. In this work, we adopt the finite element method (FEM), which can treat problems with curved material boundaries easily, to realize the IT-BPM, and analyze a square-arranged PC to show the correctness of this IT-BPM.

Formulation

For a 2D problem with geometry defined in the x-y plane, the following equation can be derived from Maxwell's equations:

$$\frac{\partial}{\partial x}\left(p\frac{\partial \Phi}{\partial x}\right)+\frac{\partial}{\partial y}\left(p\frac{\partial \Phi}{\partial y}\right)-\mu_0\epsilon_0 q\frac{\partial^2 \Phi}{\partial t^2}=0 \tag{1}$$

with $p=1/\epsilon_r$, $q=\mu_r$ for the TE mode ($\Phi=H_z$) and $p=1/\mu_r$, $q=\epsilon_r$ for the TM mode ($\Phi=E_z$), where μ_0 and ϵ_0 are, respectively, the permeability and permittivity of free space, and μ_r and ϵ_r are the relative permeability and relative permittivity of the medium, respectively.

Assuming $\Phi(x,y,t)=\phi(x,y,t)\exp(j\omega_0 t)$ and ignoring the second derivative term, Eq. (1) becomes

$$\frac{\partial}{\partial x}\left(p\frac{\partial \phi}{\partial x}\right)+\frac{\partial}{\partial y}\left(p\frac{\partial \phi}{\partial y}\right)-\mu_0\epsilon_0 q\left(j2\omega_0\frac{\partial \phi}{\partial t}-\omega_0^2\phi\right)=0. \tag{2}$$

Applying the finite element technique to the x-y plane and using the periodic boundary conditions (PBCs) as required in the 2D PC, we can obtain the following matrix equation:

$$j2\omega_0\mu_0\epsilon_0[M]\frac{d\{\phi\}}{dt}+([K]-\omega_0^2\mu_0\epsilon_0[M])\{\phi\}=\{0\} \tag{3}$$

with

$$[K]=\sum_e\int\int\left(p\frac{\partial\{N\}}{\partial y}\frac{\partial\{N\}^T}{\partial y}+p\frac{\partial\{N\}}{\partial x}\frac{\partial\{N\}^T}{\partial x}\right)dxdy \tag{4}$$

$$[M]=\sum_e\int\int q\{N\}\{N\}^T dxdy \tag{5}$$

where $\{\phi\}$ is the global electric or magnetic field vector, $\{N\}$ is the shape function vector, $\{0\}$ is a null vector, $\sum_e$ extends over all different elements, and T denotes transpose.

Utilizing the two-point recurrence scheme, Eq. (3) is written as

$$j2\omega_0\mu_0\epsilon_0[M]\frac{\{\phi\}_{i+1}-\{\phi\}_i}{\Delta t}+([K]-\omega_0^2\mu_0\epsilon_0[M])(\theta\{\phi\}_{i+1}+(1-\theta)\{\phi\}_i)=\{0\} \tag{6}$$

which can be rearranged as

$$[A]_i\{\phi\}_{i+1} = [B]_i\{\phi\}_i \tag{7}$$

with

$$[A]_i = j2\omega_0\mu_0\epsilon_0[M] + \theta\Delta t([K] - \omega_0^2\mu_0\epsilon_0[M]) \tag{8}$$

$$[B]_i = j2\omega_0\mu_0\epsilon_0[M] - (1-\theta)\Delta t([K] - \omega_0^2\mu_0\epsilon_0[M]) \tag{9}$$

where Δt is the time step size, θ is set to be 1 in our analysis, and the subscripts i and $(i+1)$ denote the quantities related to the ith and $(i+1)$th time steps, respectively.

Assuming that the frequency of the rth eigenmode is ω_r and that the corresponding field is $\{f_r\}$, they must satisfy the following equation

$$[K]\{f_r\} = \omega_r^2\mu_0\epsilon_0[M]\{f_r\}. \tag{10}$$

After a propagation time of Δt using Eqs. (7)–(10), the field distribution of the rth eigenmode yields

$$\{f_r\}_{i+1} = \frac{j2\omega_0\mu_0\epsilon_0 - (1-\theta)\Delta t(\omega_r^2\mu_0\epsilon_0 - \omega_0^2\mu_0\epsilon_0)}{j2\omega_0\mu_0\epsilon_0 + \theta\Delta t(\omega_r^2\mu_0\epsilon_0 - \omega_0^2\mu_0\epsilon_0)}\{f_r\}_i. \tag{11}$$

If m eigenmodes exist in the PC, the field $\{\phi\}_i$ at the ith time step can be expressed by

$$\{\phi\}_i = \sum_{r=1}^{m} A_{r,i}\{f_r\} \tag{12}$$

where $A_{r,i}$ is the amplitude of the rth eigenmode. Selecting Δt as

$$\Delta t \simeq -\frac{j2\omega_0}{\theta(\omega_r^2 - \omega_0^2)} \tag{13}$$

and after a sufficiently large number of i time steps, $\{\phi\}$ converges to the rth eigenvector $\{f_r\}$. The frequency of this eigenmode, ω_r, is obtained by

$$\omega_{r,i}^2 = \frac{\{\phi\}_i^\dagger[K]_i\{\phi\}_i}{\mu_0\epsilon_0\{\phi\}_i^\dagger[M]_i\{\phi\}_i} \tag{14}$$

at the ith time step with $\dagger$ denoting the complex conjugate and transpose.

As one eigenmode is solved through the process introduced above, we can obtain another eigenmode easily by using a new input field, in which the previously-solved field component is eliminated, to initiate the same process, that is, following the Gram-Schmidt process. By repeating this procedure, the band structure of a 2D PC can be constructed systematically.

Numerical Results

To demonstrate the correctness of this IT-BPM, we consider a 2D PC with square lattice, as shown in Fig. 1(a), formed by parallel alumina rods with relative permittivity $\epsilon_r = 8.9$ and radius $r = 0.2a$ in the air, where a is the lattice distance. Because of the periodic geometry of the PC, only the unit cell of the PC, as indicated by the dashed lines in Fig. 1(a), needs to be considered with the PBCs. The corresponding first Brillouin zone (BZ) of this PC structure is shown in Fig. 1(b), in which the irreducible BZ is marked by Γ-X-M.

Fig. 2(a) and (b) shows, respectively, the band structures of the TE and TM modes for this square-arranged PC. The circles denote the results obtained using the IT-BPM, and the solid lines are those calculated by the FDFD method [3]. It can be seen that the circles match quite well with the solid lines for both TE and TM modes of this PC structure, showing the reliability of the IT-BPM for the band structure analysis of 2D PCs.

Conclusion

Following the concept of the well-known ID-BPM, we have successfully developed an IT-BPM based on the FEM to calculate the band structures of 2D PCs. The formulation of this method is straightforward. Through the band structure analysis of a square-arranged PC, we can see that the results from this method agree with those from the FDFD method [3] very well, and the correctness of this work is validated clearly.

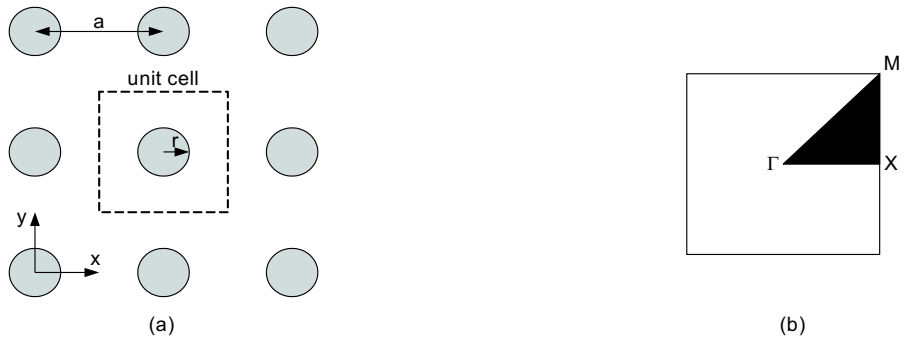

Figure 1: (a) Cross-section of the 2D PC with square lattice. (b) The first BZ of (a).

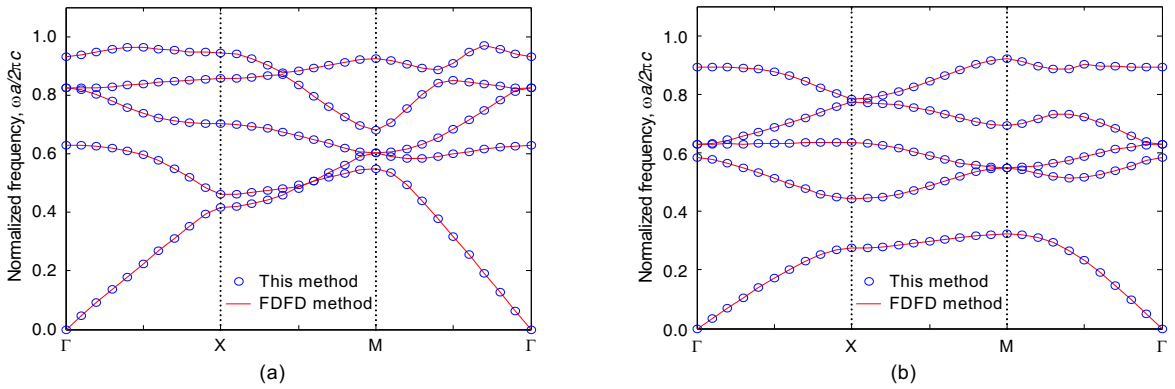

Figure 2: Band structures of (a) the TE mode and (b) the TE mode for the 2D PC with square lattice.

REFERENCES

[1] D. Yevick and B. Hermansson, "New approach to lossy optical waveguide," *Electron. Lett.* **21**, pp. 1029–1030 (1985).

[2] Y. Tsuji and M. Koshiba, "Guided-mode and leaky-mode analysis by imaginary distance beam propagation method based on finite element scheme," *J. Lightwave Technol.* **18**, pp. 618–623 (2000).

[3] C. P. Yu and H. C. Chang, "Compact finite-difference frequency-domain method for the analysis of two-dimensional photonic crystals," *Opt. Express* **12**, pp. 1397–1408, 2004.

Appendix III

MODAL ANALYSIS OF PLASMONIC WAVEGUIDES

Han-Chih Yeh[1], Chan-Huan Peng[2], Bang-Yan Lin[1], and Hung-chun Chang[1,2,3]
[1]Graduate Institute of Communication Engineering, National Taiwan University
[2]Graduate Institute of Electro-Optical Engineering, National Taiwan University
[3]Department of Electrical Engineering, National Taiwan University, Taipei, Taiwan 10617, R.O.C.
E-Mail: hcchang@cc.ee.ntu.edu.tw

Abstract: A full-vectorial imaginary-distance finite-element beam propagation method based on curvilinear hybrid edge/nodal elements with triangular shape is applied to study surface plasmon modes on plasmonic waveguides. Triangular metal wedge waveguides are in particular investigated in detail in this work by considering different wedge angles and two different wavelengths. Not only wedges rounded with an arc radius but also the ideal sharp wedges are analyzed. The latter ideal structures obviously possess better mode confinement near the tip and significantly larger losses.

1. INTRODUCTION

Surface plasmons (SPs), or surface plasma polaritons, existing at an interface between a metal and a dielectric at optical frequencies with electromagnetic fields evanescently decaying away from the interface in both media have been well-known phenomena and find many new applications in nanophotonics [1]. From the optical wave guiding viewpoint, SPs along a planar interface are two-dimensional (2-D) guided-wave modes. To make SPs more useful in optical signal transmission applications or in achieving high-degree miniaturization of integrated optical circuits, one needs 3-D waveguides with further mode field confinement in the other transverse direction. Such 3-D waveguides have recently been investigated experimentally and theoretically, including those with finite metal-strip cross-section for obtaining long-range SP modes [2]–[4] and those with a groove on a metal surface for achieving subwavelength waveguides [5]–[7]. Due to their highly localized field distribution and vector-mode characteristics at the metal-dielectric interfaces, the SP waveguides are more difficult to analyze compared to conventional optical waveguides for obtaining accurate complex propagation constants. The method of line [2], the integral equation method [5], and the finite-difference time-domain (FDTD) [6], [7] have been employed for studying 3-D SP waveguides. Recently, SPs on triangular metal wedges [7], or Λ-shaped metal corners, (called wedge plasmon polaritons) have been analyzed in detail based on the finite element method (FEM) [8]. The FEM has the advantages of better treating material interface boundary conditions through adaptive mesh distribution, as compared to traditional FD methods using orthogonal grid meshes.

We have established an imaginary-distance finite-element beam propagation method (ID-FE-BPM) for solving optical waveguide modes [9], [10], which is a suitable method for analyzing SP modes on various plasmonic waveguides. In this paper, we apply the analysis method to investigate the behavior of SP modes on triangular metal wedges [7], [8]. In [8], the triangular wedges were assumed to be rounded with an arc of 10-nm radius. Here we examine the effect of different values of such arc radius, including the ideal sharp-wedge case (zero arc radius) as shown in Fig. 1(a). We are able to do so thanks to the hybrid edge-nodal elements employed in our method.

2. THE FINITE ELEMENT MODE SOLVER

The FEM based electromagnetic solution schemes have been very powerful techniques for waveguide mode analysis. Its flexible nonuniform mesh-size assignment is particularly useful for saving memory storage. Our full-vectorial FE-ID-BPM is incorporated with perfectly matched layer (PML) absorbing boundary conditions (ABCs) for calculating the real and imaginary parts of the modal propagation constants. In the FE analysis, the waveguide cross-section is divided into curvilinear hybrid edge/nodal elements with triangular shape. Such elements are particularly useful for imposing the continuity of the tangential fields. Linear tangential and quadratic normal (LT/QN) basis functions are employed. The H-formulation is utilized. The use of the curvilinear hybrid elements makes it possible to calculate the six field components (that is, E_x, E_y, E_z, H_x, H_y, and H_z) from obtained eigenvectors, to efficiently adjust the mesh density to properly fitting the shape of the waveguide, and to derive eigenmodes without extracting spurious solutions. The flexibility of the element size also allows us to increase the mesh density in a specific area, resulting in a more accurate description of a local area without sharply increasing the computing time. With the slowly varying envelope aprroximation and the Fresnel approximation in the algorithm of the BPM, the ID-BPM can extract desired modes without directly solving the

eigenvalue equation and thus avoid the difficulty in guessing an initial value for numerical iteration. Therefore, the ID-BPM is an efficient method in analyzing a waveguide that is difficult to predict the modal index that is the propagation constant divided by the free-space wavenumber, as in the present SP problem.

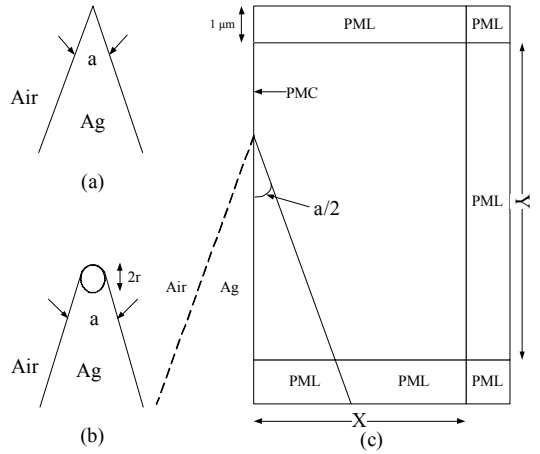

Fig. 1. (a) Sharp air/silver wedge. (b) Rounded air/silver wedge. (b) Schematic of the computational domain with PML regions.

3. THE TRIANGULAR WEDGES

We consider both the sharp and rounded air/silver wedges, as depicted in Figs. 1(a) and (b), respectively, where $2r$ in Fig. 1(b) is the diameter of the tip arc. According to the Drude model, the complex dielectric constant of silver is $-15.9149 - j0.7477$ at the wavelength, $\lambda = 0.633$ μm, and $-111.0137 - j10.5657$ at $\lambda = 1.55$ μm. Due to the geometrical symmetry, we can consider only half of the cross-section with the symmetry plane replaced with a perfect magnetic conductor (PMC), as indicated in the computational domain shown in Fig. 1(c), where PML regions of thickness 1 μm are placed around the three sides. Fig. 2 shows the mesh division of the computational domain for the case of a sharp wedge with angle $\alpha = 50^\circ$, with X = 3 μm and Y = 6 μm in Fig. 1(c). The number of unknowns corresponding to the division shown is 24764. Fig. 3 shows the enlarged views of the mesh near the wedge tip when the numbers of unknowns are 8899, 9945, 24764, respectively. The triangle side length can be as small as 1 nm near the tip. To examine numerical convergence of the calculated SP modal index versus the number of unknowns, we use the $\alpha = 50^\circ$ case as an example and the obtained results are plotted in Fig. 4 for r = 0, 5, and 10 nm, where the effective index means the real part of the modal index and the loss in dB/mm is derived from the imaginary part of the modal index. Good convergence behavior is seen for each line.

With carefully checked numerical convergence, we obtain the effective-index and loss characteristics versus the wedge angle, α, for r = 0, 5, and 10 nm at $\lambda = 0.633$ μm and 1.55 μm, and are presented in Fig. 5. The r = 10 nm results agree with those presented in [8]. It is seen that at smaller wedge angles, the modal index characteristics depend drastically upon the r value. As r decreases, the mode is more localized near the tip top as evidenced by the increase in the effective index, while the modal loss gets larger much rapidly.

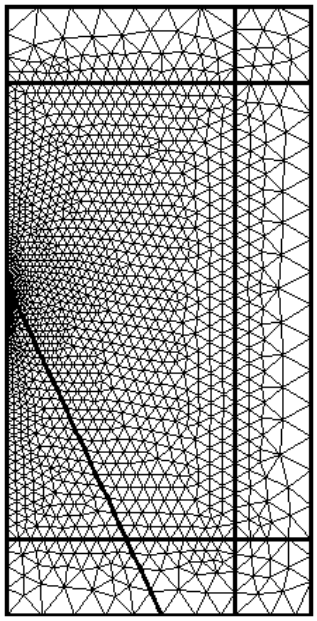

24764 unknowns

Fig. 2. Finite element mesh division for the computational domain for the case of a sharp wedge with angle $\alpha = 50^\circ$.

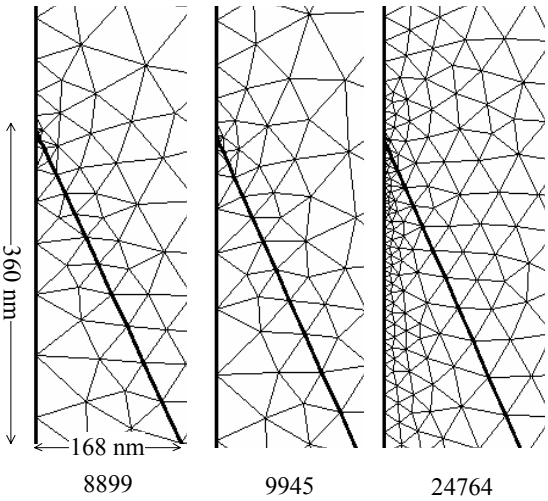

Fig. 3. Enlarged views of the mesh near the wedge tip when the numbers of unknowns are 8899, 9945, 24764, respectively.

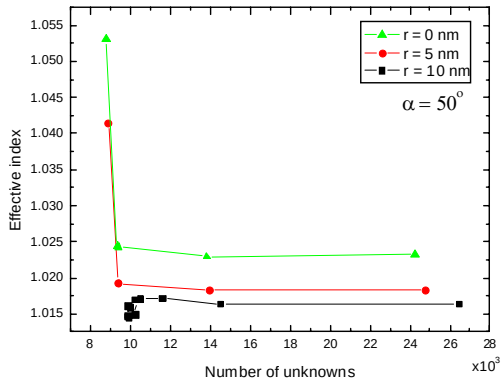

(a)

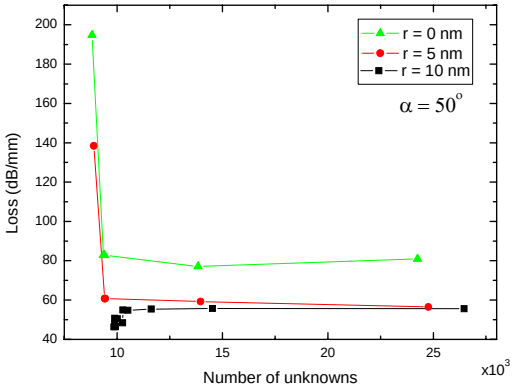

(b)

Fig. 4. Numerical convergence of the calculated SP (a) effective index and (b) loss versus the number of unknowns.

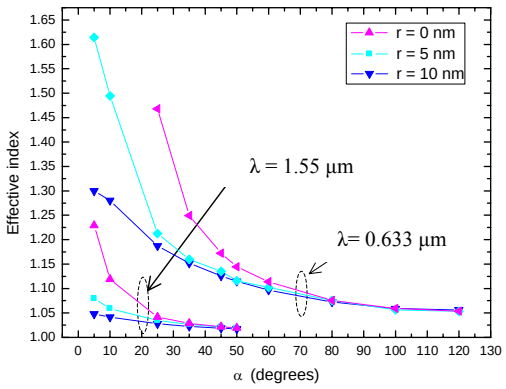

(a)

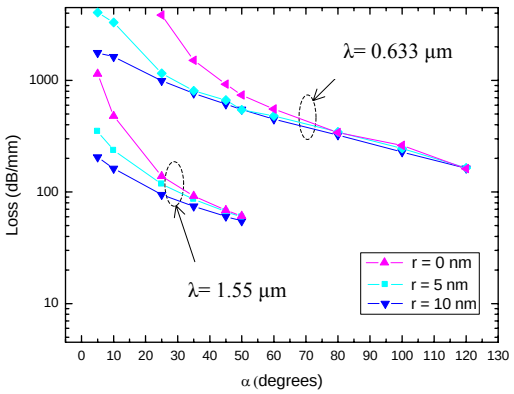

(b)

Fig. 5. (a) The effective-index and (b) the loss characteristics of SPs versus the wedge angle for different r values at $\lambda = 0.633$ and 1.55 μm.

We examine in detail the mode field profiles among different r values for the structure of $\alpha = 25^\circ$ at $\lambda = 1.55$ μm. Fig. 6 shows the H_x profile along the y axis. With the inset, the wedge tip tops that are located at $y = 0.3600$ μm, 0.3419 μm, 0.323 μm, respectively, are marked by the three corresponding arrows. Although the maximum of H_x occurs at the tip top for both $r = 5$ nm and 10 nm cases, it is not the situation for the $r = 0$ nm structure for which it is observed that the maximum occurs below the tip with the ratio of the H_x magnitudes at these two locations being 1.03 : 0.982. It is interesting to see that the field profile is wider for the $r = 0$ nm structure, revealing better localization of the SP mode. We also present in Fig. 7 the corresponding H_x, H_y, and H_z profiles along the horizontal lines passing respective wedge tip tops for the three different r cases. The profiles for $r = 0$ nm obviously have larger peaks. Note that H_x is symmetric with respect to $y = 0$ while H_y and H_z are anti-symmetric. Finally, the H_x, H_y, and H_z contours in the x-y plane for the $\alpha = 25$ and $r = 0$ nm structure at $\lambda = 1.55$ μm are plotted respectively in the three panels of Fig. 8.

4. CONCLUSION

We have employed a full-vectorial ID-FE-BPM based on curvilinear hybrid edge/nodal elements with triangular shape to study SP modes on plasmonic waveguides. The complex modal propagation constants are accurately obtained with their real parts giving modal dispersion characteristics and the imaginary parts predicting the losses. We have in particular investigated in detail triangular metal wedge waveguides by considering different wedge angles and two different wavelengths at 0.633 μm and 1.55 μm, as in [8]. We, however, have analyzed not only wedges rounded with an arc radius but also the ideal sharp wedges. It is observed that the latter ideal structures obviously possess better mode confinement near the tip and significantly larger losses.

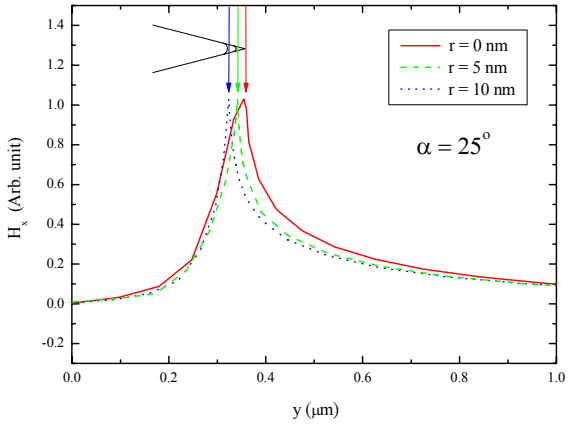

Fig. 6. The H_x profile along the y axis for the structure of $\alpha = 25^\circ$ at $\lambda = 1.55$ μm. The wedge tip tops, as illustrated in the inset that are located at $y = 0.3600$ μm, 0.3419 μm, 0.323 μm, respectively, are marked by the three corresponding arrows.

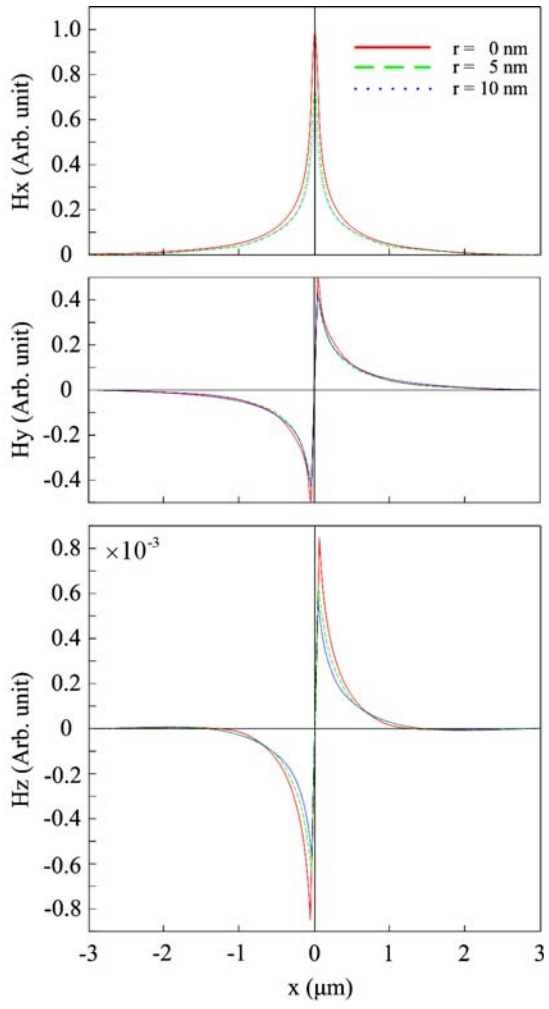

Fig. 7. Corresponding H_x, H_y, and H_z profiles along the horizontal lines passing respective wedge tip tops for the three different r cases.

ACKNOWLEDGEMENT

This work was supported in part by the National Science Council of the Republic of China under grant NSC95-2221-E-002-328, in part by the Ministry of Economic Affairs of the Republic of China under grant 95-EC-17-A-08-S1-0006, in part by the Excellent Research Projects of National Taiwan University under grant 95R0062-AE00-06, and in part by the Ministry of Education of the Republic of China under "The Aim of Top University Plan" grant.

REFERENCES

[1] H. Raether, *Surface Plasmons*, Berlin: Springer-Verlag, 1988.

[2] P. Berini, "Plasmon-polariton modes guided by a metal film of finite width," *Opt. Lett.*, vol. 24, pp. 1011–1013, 1999.

[3] R. Charbonneau, P. Berini, E. Berolo, and E. Lisicka-Shrzek, "Experimental observation of Plasmon-polariton waves supported by a thin metal film of finite width," *Opt. Lett.*, vol. 25, pp. 844–846, 2000.

[4] P. Berini, "Plasmon-polariton waves guided by thin lossy metal films of finite width: Bound modes of symmetric structures," *Phys. Rev. B.*, vol. 61, pp. 10484–10503, 2000.

[5] I. V. Novikov and A. A. Maradudin, "Channel polaritons," *Phys. Rev. B.*, vol. 66, 035403, 2002.

[6] D. F. P. Pile and D. K. Gramotnev, "Channel plasmon-polariton in a triangular groove on a metal surface," *Opt. Lett.*, vol. 29, pp. 1069–1071, 2004.

[7] D. F. P. Pile, T. Ogawa, D. K. Gramotnev, T. Okamoto, M. Haraguchi, M. Fukui, and S. Matsuo, "Theoretical and experimental investigation of strongly localized plasmons on triangular metal wedges for subwavelength waveguiding," *Appl. Phys. Lett.*, vol. 87, 061106, 2005.

[8] M. Yan and M. Qiu, "Finite-element analysis of Λ-wedge plasmon polariton guide," *Proc. the 13th European Conference on Integrated Optics (ECIO 2007)*, paper THG35, April 2007.

[9] K. Saitoh and M. Koshiba, "Full-vectorial imaginary-distance beam propagation method based on a finite element scheme: Application to photonic crystal fiber" *IEEE J. Quantum Electron.*, vol. 38, pp. 917–933, 2002.

[10] S. M. Hsu, H. J. Chen, and H. C. Chang, "Finite element analysis of full-vectorial modal and leakage properties of microstructured and photonic crystal fibers," *Proc. SPIE*, Vol. 5623, pp. 316–324, 2005.

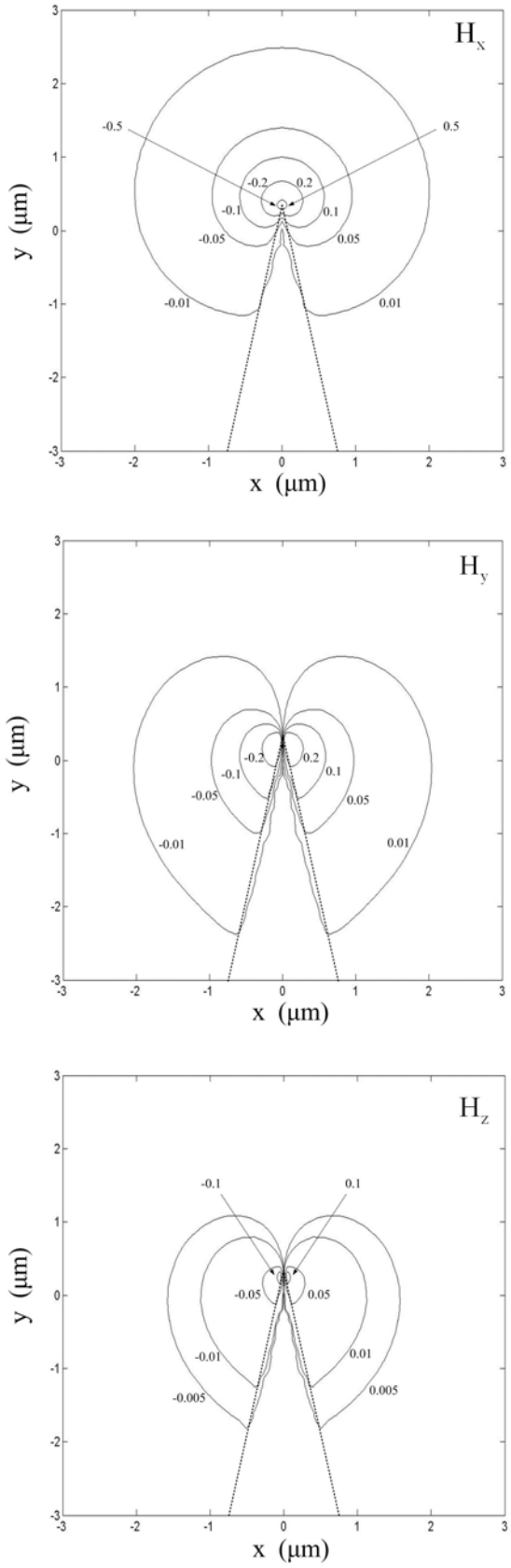

Fig. 8. The H_x, H_y, and H_z contours in the x-y plane for the $\alpha = 25^\circ$ and $r = 0$ nm structure at $\lambda = 1.55$ μm.